AD-A038 686 STANFORD RESEARCH INST MENLO PARK CALIF F/G 11/2
CHARACTERIZATION OF THE DYNAMIC BEHAVIOR OF POROUS SOLIDS. VOLU--ETC(U)
MAR 76 A B LUTZE, M J GINSBERG, D R CURRAN DNA001-74-C-0150
UNCLASSIFIED DNA-3961F-4 NL

| OF |
AD
A038686

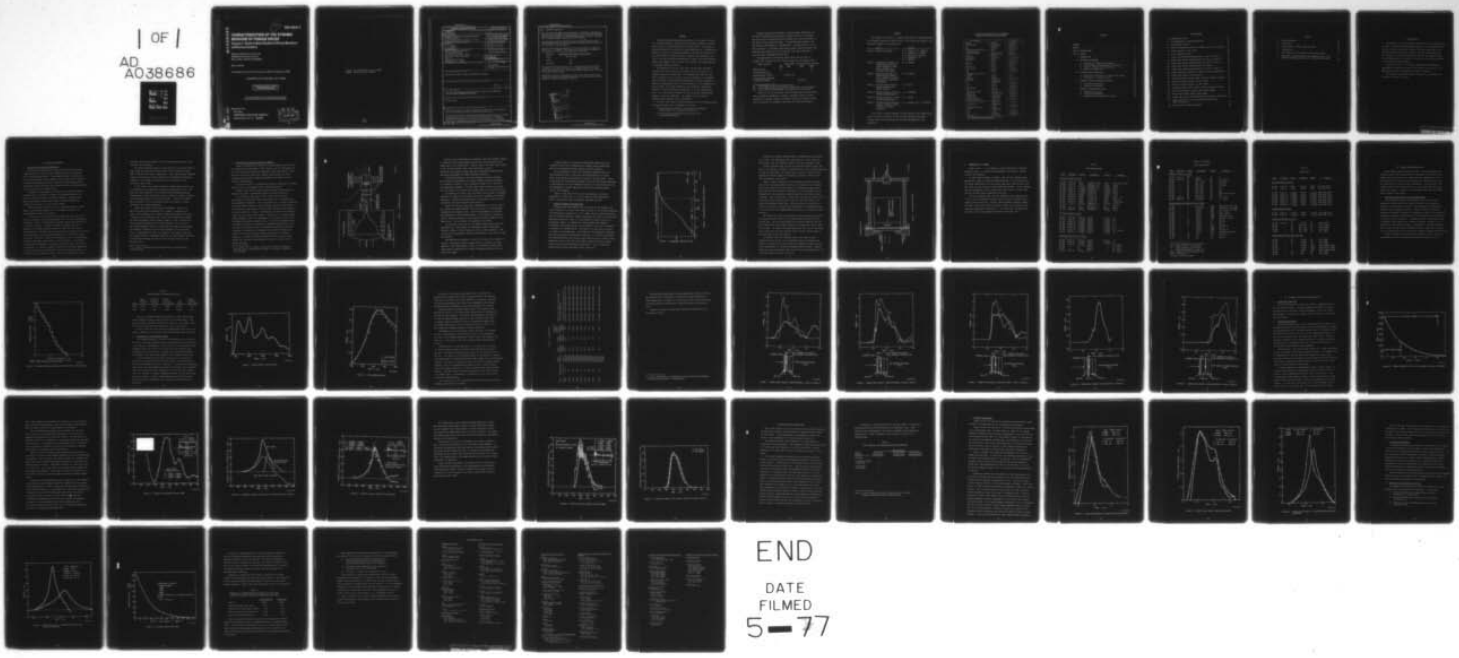

END

DATE
FILMED
5-77

AD A038686

DNA 3961F-4

# CHARACTERIZATION OF THE DYNAMIC BEHAVIOR OF POROUS SOLIDS

## Volume 4 - Electron Beam Studies of Porous Beryllium and Porous Ceramics

Stanford Research Institute
333 Ravenswood Avenue
Menlo Park, California 94025

March 1976

Final Report for Period 14 January 1974—31 January 1976

CONTRACT No. DNA 001-74-C-0150

APPROVED FOR PUBLIC RELEASE;
DISTRIBUTION UNLIMITED.

THIS WORK SPONSORED BY THE DEFENSE NUCLEAR AGENCY
UNDER RDT&E RMSS CODE B342076464 N99QAXAC30840 H2590D.

Prepared for
Director
DEFENSE NUCLEAR AGENCY
Washington, D. C. 20305

DDC FILE COPY
NO.

DDC
RECEIVED
APR 27 1977
A

Destroy this report when it is no longer needed. Do not return to sender.

DNA PRINTING PLANT

UNCLASSIFIED

SECURITY CLASSIFICATION OF THIS PAGE *(When Data Entered)*

| REPORT DOCUMENTATION PAGE | | READ INSTRUCTIONS BEFORE COMPLETING FORM |
|---|---|---|
| 1. REPORT NUMBER<br>DNA 3961F-4 | 2. GOVT ACCESSION NO. | 3. RECIPIENT'S CATALOG NUMBER |
| 4. TITLE *(and Subtitle)*<br>CHARACTERIZATION OF THE DYNAMIC BEHAVIOR OF POROUS SOLIDS.<br>Volume 4. Electron Beam Studies of Porous Beryllium and Porous Ceramics. | | 5. TYPE OF REPORT & PERIOD COVERED<br>Final Report for Period<br>14 Jan 74—31 Jan 76<br>6. PERFORMING ORG. REPORT NUMBER<br>SRI Project PYU-3163 |
| 7. AUTHOR(s)<br>A. B. Lutze<br>M. J. Ginsberg<br>D. R. Curran | | 8. CONTRACT OR GRANT NUMBER(s)<br>DNA 001-74-C-0150 |
| 9. PERFORMING ORGANIZATION NAME AND ADDRESS<br>Stanford Research Institute<br>333 Ravenswood Avenue<br>Menlo Park, California 94025 | | 10. PROGRAM ELEMENT, PROJECT, TASK AREA & WORK UNIT NUMBERS<br>Subtask N99QAXAC308-40 |
| 11. CONTROLLING OFFICE NAME AND ADDRESS<br>Director<br>Defense Nuclear Agency<br>Washington, D.C. 20305 | | 12. REPORT DATE<br>March 1976<br>13. NUMBER OF PAGES<br>62 |
| 14. MONITORING AGENCY NAME & ADDRESS*(if different from Controlling Office)* | | 15. SECURITY CLASS *(of this report)*<br>UNCLASSIFIED<br>15a. DECLASSIFICATION DOWNGRADING SCHEDULE |

16. DISTRIBUTION STATEMENT *(of this Report)*

Approved for public release; distribution unlimited.

17. DISTRIBUTION STATEMENT *(of the abstract entered in Block 20, if different from Report)*

332 500

18. SUPPLEMENTARY NOTES

This work sponsored by the Defense Nuclear Agency under RDT&E RMSS Code B342076464 N99QAXAC30840 H2590D.

19. KEY WORDS *(Continue on reverse side if necessary and identify by block number)*

Electron Beam

20. ABSTRACT *(Continue on reverse side if necessary and identify by block number)*

This work was part of a two-year program to characterize the response of porous, refractory materials to rapid energy deposition.

The objective of the electron-beam experiments reported here was to obtain stress-time profiles for porous ceramics and beryllium in the high internal-energy region of the equation-of-state surface. Stress-time profiles or, alternatively, particle velocity histories were recorded

over

DD FORM 1 JAN 73 1473 EDITION OF 1 NOV 65 IS OBSOLETE

UNCLASSIFIED

SECURITY CLASSIFICATION OF THIS PAGE *(When Data Entered)*

20. ABSTRACT (Continued)

with piezoresistive gages and interferometric techniques, respectively. Test materials selected for characterization were (1) sintered and flame-sprayed alumina ($Al_2O_3$), (2) plasma-sprayed aluminum titanate ($Al_2TiO_5$), and (3) plasma-sprayed distended beryllium (PSDB).

Two additional forms of distended beryllium (sintered beryllium and plasma-sprayed beryllium) were provided by Lawrence Livermore Laboratory (LLL) and tested in this program.

Electron-beam energy was deposited in the test materials to depths of roughly 0.4 - 0.6 gm/cm$^2$. The front-surface dose levels accompanying the irradiation of the test materials were as follows:

| Material | Approximate Front-Surface Dose (cal/cm) |
|---|---|
| $Al_2O_3$ | 500 and 2000 |
| $Al_2TiO_3$ | 700 |
| Beryllium | 1000 |

The particular dose levels for each of the materials were dictated by the needs of the analytical effort. For example, data in the vapor region were needed for $Al_2O_3$ but melt-dominated response was of interest for $Al_2TiO_5$ and beryllium.

Depth-dose profiles are presented for each of the front surface dose conditions together with energy deposition rate curves and the recorded histories of stress and particle velocity.

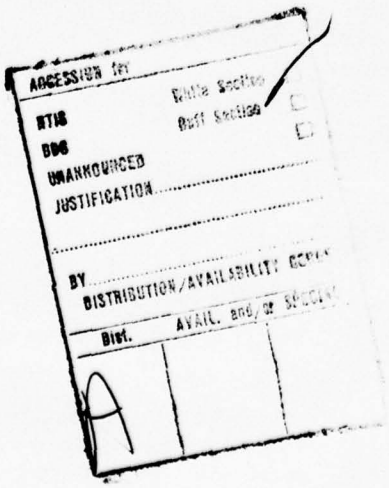

## SUMMARY

The electron-beam experiments described in this report were part of a two-year program to characterize the dynamic response of certain porous solids to sudden deposition of radiant energy. The method of characterization was to construct a model consisting of a thermodynamic equation of state and including mechanical constitutive relations for the test materials (alumina, aluminum titanate, and beryllium), and then to use these analytical mechanisms to compute the stress histories (hence, also impulse) and the final states (hence, also spall depths) of irradiated porous materials.

The procedure was to use impact data and the model parameters available from the literature to construct the best estimate for a complete equation-of-state model. Wave propagation codes were then used to compute stress or particle velocity histories to be compared with the results of electron-beam experiments which were designed to explore the high-energy states of test materials. This comparison was used to adjust the initial Grüneisen ratio estimates, sublimation energies, and other vapor-state parameters to fit the electron beam data. As a final step, the model was used to predict UGT-generated response of the test materials. The success of this method is presented under separate cover (see PREFACE).

In short, the utility of electron-beam data in the characterization of porous materials was to determine or to verify

- The porous yield surface in the absence of Grüneisen ratios, moduli, or strength reduction data.
- The fully dense equation-of-state surface near initial porous density.

Although irradiation conditions in electron-beam experiments are ultimately compromises between what is needed and what is available, the dose levels and energy penetration depths were chosen according to the needs of the analytical effort. The electron-beam generator was The Physics International Co. 738 Pulserad. Its pulse history can be seen in Figure 2. The energy penetration depths (electron ranges) were generally kept between 0.4 and 0.6 gm/cm$^2$, with some variations to suit particular experimental geometries.

The approximate front-surface (peak) doses and the types of response data obtained for the several materials in the program were:

| Target Material | Approximate Front-Surface Dose (cal/gm) | | | |
|---|---|---|---|---|
| | 500 | 700 | 1000 | 2000 |
| Sintered $Al_2O_3$ | CG | | | CG |
| Flame-Sprayed $Al_2O_3$ | | | | CG |
| Plasma-Sprayed $Al_2TiO_3$ | | CG, LDI, LVI | | |
| Plasma-Sprayed Distended Beryllium (PSDB) | | | CG, LDI, LVI | |

CG = Carbon gage (in-material configuration)
LDI = Laser displacement interferometer (measurement in fused quartz)
LVI = Laser velocity interferometer (measurement in fused quartz)

Figures 4, 12, 22, and Table 4 give the depth-dose information for these irradiation conditions. Figures 5 through 11 plot the stress histories of alumina; Figures 13 through 17 show the aluminum titanate data; and Figures 18 through 21 illustrate the beryllium response.

## PREFACE

This report is Volume 4 of a seven-volume series on Characterization of the Dynamic Behavior of Porous Solids. The titles and authors of the individual reports in the series are:

| | Title | Authors |
|---|---|---|
| Volume 1 | Summary of Results | D. R. Curran, R. E. Tokheim, M. J. Ginsberg, L. Seaman, A. B. Lutze, D. C. Erlich, J. T. Rosenberg, and D. A. Shockey |
| Volume 2 | Computational Models for Predicting the Dynamic Stress Response of Some Porous Ceramics in a Radiation Environment | R. E. Tokheim |
| Volume 3 | Computational Model for Predicting the Dynamic Stress Response of Porous Beryllium in a Radiation Environment | R. E. Tokheim |
| Volume 4 | Electron Beam Studies of Porous Beryllium and Porous Ceramics | A. B. Lutze |
| Volume 5 | Dynamic Response of Porous Beryllium--Experiments | J. T. Rosenberg |
| Volume 6 | Dynamic Response of Porous Ceramics--Experiments | D. C. Erlich |
| Volume 7 | Microstructural Characterization of Several Porous Ceramics and Porous Beryllium | D. A. Shockey and J. P. Wilhelm |

The author is deeply indebted to Sergei Heurlin, and Gordon Harvey of PI, and to Mr. Lee Hall, of SRI, for the numerous hours spent between sunset and dawn wooing the electron-beam generator into submission.

## Conversion factors for U.S. customary to metric (SI) units of measurement.

| To Convert From | To | Multiply By |
|---|---|---|
| angstrom | meters (m) | 1.000 000 X E -10 |
| atmosphere (normal) | kilo pascal (kPa) | 1.013 25 X E +2 |
| bar | kilo pascal (kPa) | 1.000 000 X E +2 |
| barn | meter$^2$ (m$^2$) | 1.000 000 X E -28 |
| British thermal unit (thermochemical) | joule (J) | 1.054 350 X E +3 |
| calorie (thermochemical) | joule (J) | 4.184 000 |
| cal (thermochemical)/cm$^2$ | mega joule/m$^2$ (MJ/m$^2$) | 4.184 000 X E -2 |
| curie | *giga becquerel (GBq) | 3.700 000 X E +1 |
| degree (angle) | radian (rad) | 1.745 329 X E -2 |
| degree Fahrenheit | degree kelvin (K) | $t_K = (t°f + 459.67)/1.8$ |
| electron volt | joule (J) | 1.602 19 X E -19 |
| erg | joule (J) | 1.000 000 X E -7 |
| erg/second | watt (W) | 1.000 000 X E -7 |
| foot | meter (m) | 3.048 000 X E -1 |
| foot-pound-force | joule (J) | 1.355 818 |
| gallon (U.S. liquid) | meter$^3$ (m$^3$) | 3.785 412 X E -3 |
| inch | meter (m) | 2.540 000 X E -2 |
| jerk | joule (J) | 1.000 000 X E +9 |
| joule/kilogram (J/kg) (radiation dose absorbed) | Gray (Gy) | 1.000 000 |
| kilotons | terajoules | 4.183 |
| kip (1000 lbf) | newton (N) | 4.448 222 X E +3 |
| kip/inch$^2$ (ksi) | kilo pascal (kPa) | 6.894 757 X E +3 |
| ktap | newton-second/m$^2$ (N-s/m$^2$) | 1.000 000 X E +2 |
| micron | meter (m) | 1.000 000 X E -6 |
| mil | meter (m) | 2.540 000 X E -5 |
| mile (international) | meter (m) | 1.609 344 X E +3 |
| ounce | kilogram (kg) | 2.834 952 X E -2 |
| pound-force (lbs avoirdupois) | newton (N) | 4.448 222 |
| pound-force inch | newton-meter (N·m) | 1.129 848 X E -1 |
| pound-force/inch | newton/meter (N/m) | 1.751 268 X E +2 |
| pound-force/foot$^2$ | kilo pascal (kPa) | 4.788 026 X E -2 |
| pound-force/inch$^2$ (psi) | kilo pascal (kPa) | 6.894 757 |
| pound-mass (lbm avoirdupois) | kilogram (kg) | 4.535 924 X E -1 |
| pound-mass-foot$^2$ (moment of inertia) | kilogram-meter$^2$ (kg·m$^2$) | 4.214 011 X E -2 |
| pound-mass/foot$^3$ | kilogram/meter$^3$ (kg/m$^3$) | 1.601 846 X E +1 |
| rad (radiation dose absorbed) | **Gray (Gy) | 1.000 000 X E -2 |
| roentgen | coulomb/kilogram (C/kg) | 2.579 760 X E -4 |
| shake | second (s) | 1.000 000 X E -8 |
| slug | kilogram (kg) | 1.459 390 X E +1 |
| torr (mm Hg, 0° C) | kilo pascal (kPa) | 1.333 22 X E -1 |

*The becquerel (Bq) is the SI unit of radioactivity; 1 Bq = 1 event/s.
**The Gray (Gy) is the SI unit of absorbed radiation.

2

CONTENTS

ILLUSTRATIONS

TABLES

# I INTRODUCTION

The purpose of the electron-beam experiments was to provide stress-time data in the high internal-energy region of the equation-of-state surface. Stress, or particle velocity, histories, generated in the test materials (beryllium and ceramics) by rapid energy deposition, were recorded in two dose regimes--near melt and for aluminum oxide, in the vapor region--as dictated by the needs of the analytical effort to characterize these materials.

Sections III and IV of the report describe the electron-beam experiments and present the data on the ceramic test materials. The experiments and data on beryllium are given in Section V.

The technical background common to both sets of experiments is presented in Section II, below.



PRECEDING PAGE BLANK-NOT FILMED

## II TECHNICAL BACKGROUND

### A. Selection of Irradiation Conditions

The test materials selected for characterization require high-energy densities to reach melt and vaporization; they also possess fast stress-unloading speeds. These properties made it necessary to select electron beams with the highest total energy content available to reach the high-energy densities required for phase changes while irradiating targets over areas large enough to ensure one-dimensionality of stress waves during recording time.

Furthermore, anticipation of structure in the generated stress histories made it desirable to deposit electron-beam energy to the greatest available depths in the target materials. Deeper energy deposition generates wider stress pulses, thereby enhancing the resolution of detail in the stress-time record.

These constraints, together with its convenient proximity, made Physics International Company (PI), San Leandro, California, the electron-beam facility of our choice.

At the start of the program, the projected specification of the PI OWL II generator (1.0 MeV mean-energy, 50 kJ, 50 nsec) appeared very desirable, at least for experiments requiring substantial vaporization of the test material. With 80% transport efficiency, the OWL II promised, for example, peak dose levels of 3000 cal/g with 2-μsec one-dimensional read-times even for stress-relief velocities of 1 cm/μsec. For these reasons, we urged the development of the so-called "small-area beam" on the OWL II generator and planned to use it for experiments requiring substantial vaporization of test materials. For low-dose, long read-time measurements, relatively less total energy in the beam is required. We therefore planned to perform the near-melt experiments on the PI 738 Pulserad at nominally 0.75 MeV mean electron energy. As it turned out, the small-area beam on the OWL II generator was never

realized, and the data obtained on the PI 738 Pulserad proved to meet the needs of our program.

The energy densities required to melt both of the ceramic materials under study are below 850 cal/gm, whereas beryllium begins and ends melt at 880 and 1200 cal/gm, respectively. Thus, the near-melt condition could be satisfied for all test materials by two separate irradiation conditions; for example, one near 800 cal/gm; the other, in the vicinity of 1200 cal/gm.

At the start of our study the highest available dose level on the PI 738 Pulserad was roughly 860 cal/gm over approximately 7 $cm^2$. The peak dose value quoted by PI was inferred from mean-electron-energy consideration, without knowing the effect of magnetic focusing transport on the incidence angles of the beam electrons. In short, the needed 800 cal/gm level was far from characterized with respect to radial uniformity and in-depth description.

Higher dose levels had not yet been attempted. However, the 860 cal/gm level had been reached with a modest 1.4 magnetic lens ratio, which according to PI, could be enhanced several-fold by using a larger, existing capacitor bank to drive the solenoid that supplies the external magnetic field for beam transport. Thus, a higher dose station appeared possible on the PI 738 Pulserad with the use of a more intense magnetic lens, by varying some half-dozen beam generation and transport parameters until the best uniformity over the largest area at a prescribed dose level was achieved. This higher dose level was realized through a subprogram funded by Air Force Weapons Laboratory in 1973,[1] thus providing the second of the two dose stations in the near-melt zone.

---

[1] A. B. Lutze, "High-Dose Beam Characterization," PL-TN-2407-14-1, September 1973.

B. Electron-Beam-Loading Diagnostics Approach

Figure 1 schematically illustrates the experimental setup used for all electron beam experiments in this program. The PI 738 Pulserad was the radiation source, generating nominally 750-keV mean kinetic energy electrons which were fired into a magnetic lens through two 5-mil carbon scattering foils intended to homogenize the radial intensity (fluence) distribution.

To vary dose levels, we manipulated fluence by changing the cathode emission area and the magnetic lens focusing parameters.

Figure 1 shows that the beam transport region, between anode and target, might have a considerable effect on the beam electrons.

The scattering foils did, in fact, remove small hot spots, presumably by redirecting electron trajectories or by absorbing some beam components altogether. Also, the presence of a strongly converging, externally applied magnetic field introduced additional uncertainties in estimating average angles with which beam electrons would impinge on the front surface of a target. Furthermore, the voltage was monitored across the entire diode (see Figure 1), giving rise to a large induced voltage component which was superimposed, in the monitor record, over the needed accelerating voltage signal. All these circumstances made it somewhat hazardous to ascertain the electron beam spectrum, at the location of the target relying on information obtained in the diode. Therefore, we decided not to implement the so-called "Faraday Cup" method[2] for calculating energy deposition profiles in irradiated materials. In short, electronic diagnostic devices stood on shaky grounds and "one-shot" depth dosimeters could not survive even the low-dose station.

---

[2] V. L. Bailey and A. B. Lutze, "Mixed Phase Effects in Aluminum," PIFR-246, Physics International Company, San Leandro, California February 1972.

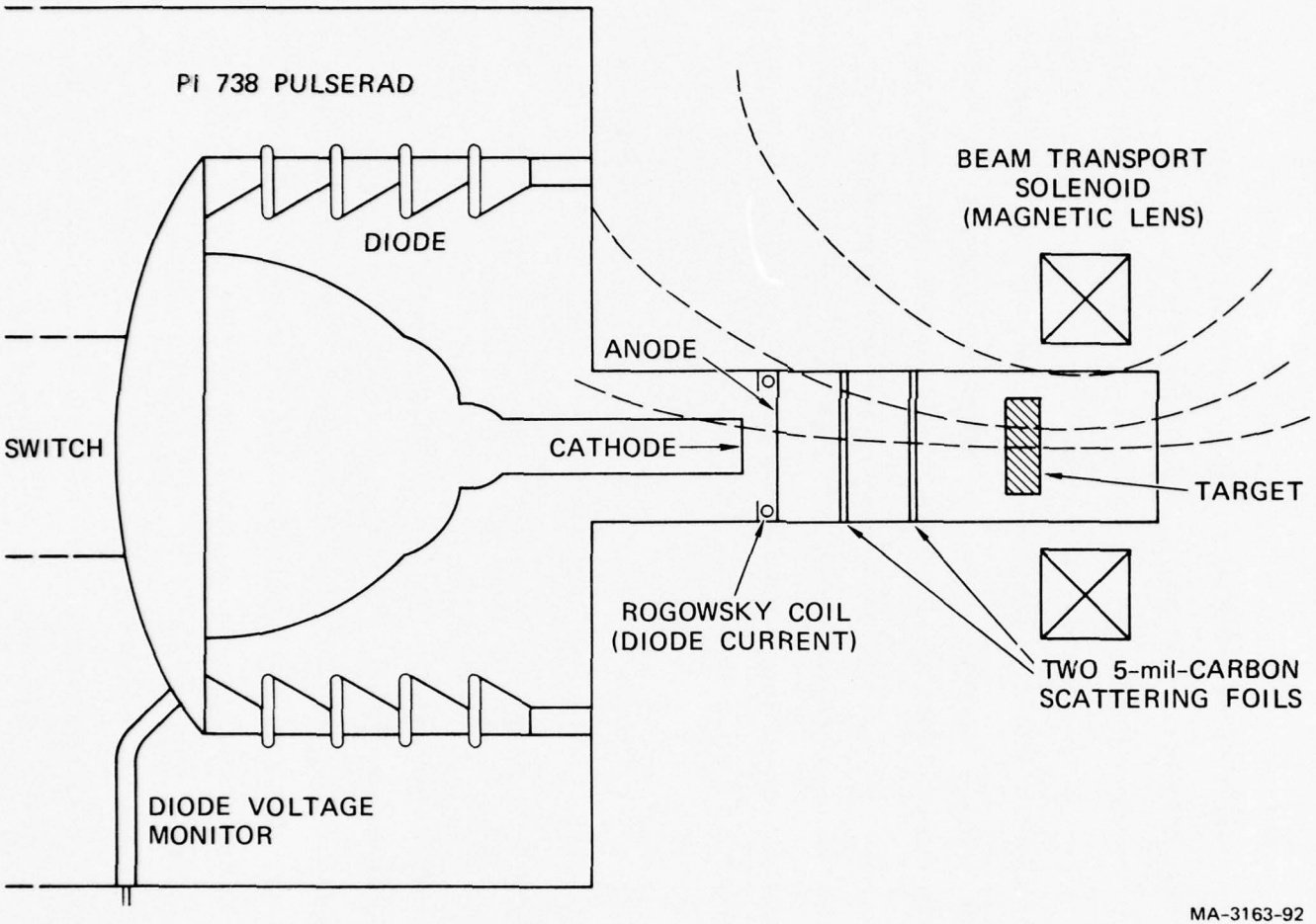


FIGURE 1 EXPERIMENTAL SETUP

Because of the uncertainties introduced by the beam transport region, we wanted to derive energy deposition profiles from measurements performed only in the target plane. However, even at the lower (800 cal/gm) of the two dose stations used in the experiments, graphite spallation and thermal cracking would have invalidated graphite depth-dose-array measurements of energy deposition profiles.

We, therefore decided to use the transmitted fluence technique[1], which relies on measurements of fluence through increasing thicknesses of a diagnostic material, such as graphite, chosen for its high melt and vaporization energies. The dose versus depth profile is obtained from the slope of the fluence versus depth curve at the target location.

As described in Section II-C, the targets were encased in shielding canisters to suppress the electrical noise that accompanies pulsed-beam generation. During the diagnostic shots, the graphite filters and the calorimeters were placed inside these canisters.

Because of the small beam spots (approximately 1.0-1.25-in. diam), the transmitted fluence method yields only one pair of fluence-depth coordinates per diagnostic shot. Since the performance of electron-beam generators is often nonrepeatable, a large number of diagnostic shots is needed to generate a statistically satisfying fluence-versus-depth curve. This is exactly the approach we have taken.

For each dose level, the set of material response data shots was accompanied by a large number of transmitted fluence measurements; typically, twenty to forty diagnostic shots per dose condition. Both the data and the diagnostic shots were replicated as many times as funds would permit.

The replication allowed us to sort all the shots into typical and atypical irradiation condition groups based on evaluation of diode monitors. With these groups of shots, we constructed a dose versus depth profile representing the typical irradiation condition for the sorted data shots.

A limited number of filtered and unfiltered Faraday-Cup shots, performed in each set of experiments as backup, proved superfluous because the transmitted fluence method was always adequate.

The dose profiles derived from transmitted fluence curves are time-integrated; that is, they give the energy density at a given depth in the material accumulated at the end of the beam pulse. Since we performed all irradiation experiments on the PI 738 Pulserad operating at approximately the same accelerating voltage, we have assumed that the time dependence of energy deposition followed the normalized power curve of that machine.

Figure 2 shows the fraction of the total energy in the beam generated at a given time, t. We have used this time dependence as input to hydrodynamic code calculations modelling the data.

C. Material Response Instrumentation

Although laser interferometry was used later in this program, our initial decision was to use stress gages, because of the relative simplicity in collecting and reducing data. Also, gages could be sandwiched between slabs of identical material, thereby minimizing the effects of acoustically mismatched interfaces, such as at the boundary of opaque targets and transparent backers, as required for interferometric measurements. Furthermore, since gages measure stress directly, their use was expected to simplify data interpretation. Our choice of stress gages was based on a number of considerations. The economy of one-dimensional hydrocode calculation requires one-dimensional input data. In stress measurements, this requirement means that radial relief from the edge of radiant energy deposition must not reach the gage elements before the axially moving stress pulse has passed through the gage plane. Thus, a small gage element would be more advantageous than a large one.

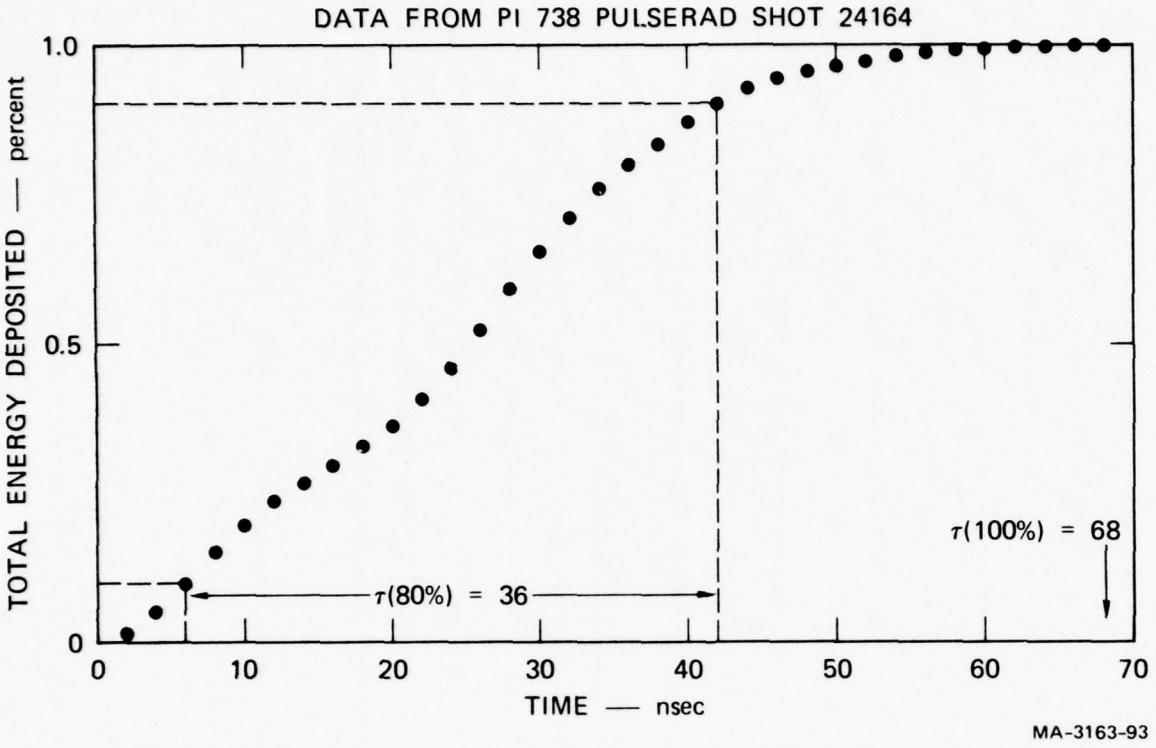


FIGURE 2 TIME-DEPENDENCE OF ENERGY DEPOSITION

Generation of pulsed electron beams is accompanied by high levels of RF noise. The chosen gage must therefore have a large signal-to-noise ratio, from the subkilobar range to the tens-of-kilobar range.

Because resistive gage circuits are effective pick-up loops, and, most of the materials intended for characterization were either dielectrics or very poor conductors, the target slabs in front of gages were not expected to provide enough RF shielding to guarantee suitably noise-free recording of stress waves.

Figure 3 shows a schematic of the shielding canister ultimately used for all the electron-beam testing in this program. This canister essentially encloses the stress gage in a conducting cylinder, whose walls and rear lid are thick with respect to the RF frequency but are transparent to the externally impressed magnetic field used for beam transport. From the beam side, at the front, the gage is covered by an acoustically thin conducting foil located at the rear surface of an electron-range-thick target slab. This particular foil location was chosen in an effort to minimize the possibility of any charge buildup at the tail end of the energy deposition profile of a dielectric target material.

Our intent was to let the acoustically thin conducting foil work in conjunction with a buffer of suitable thickness between the foil and the gage. The foil would reduce the RF-signal amplitude, and the buffer would delay stress pulse arrival at the gage until the RF noise had subsided. Of course, the buffer delay plus the width of the stress pulse would have to be less than the time of radial relief arrival at the outer edge of the gage element.

The initial tests (3.5 pulsing shifts) were aimed at noise suppression, with the use of the shielding canister described above. Manganin, ytterbium, and carbon gages were compared in preparation for stress measurements in sintered and plasma-sprayed alumina. Although some quartz gage measurements were also tried in later experiments, the carbon gage proved the best for our use.

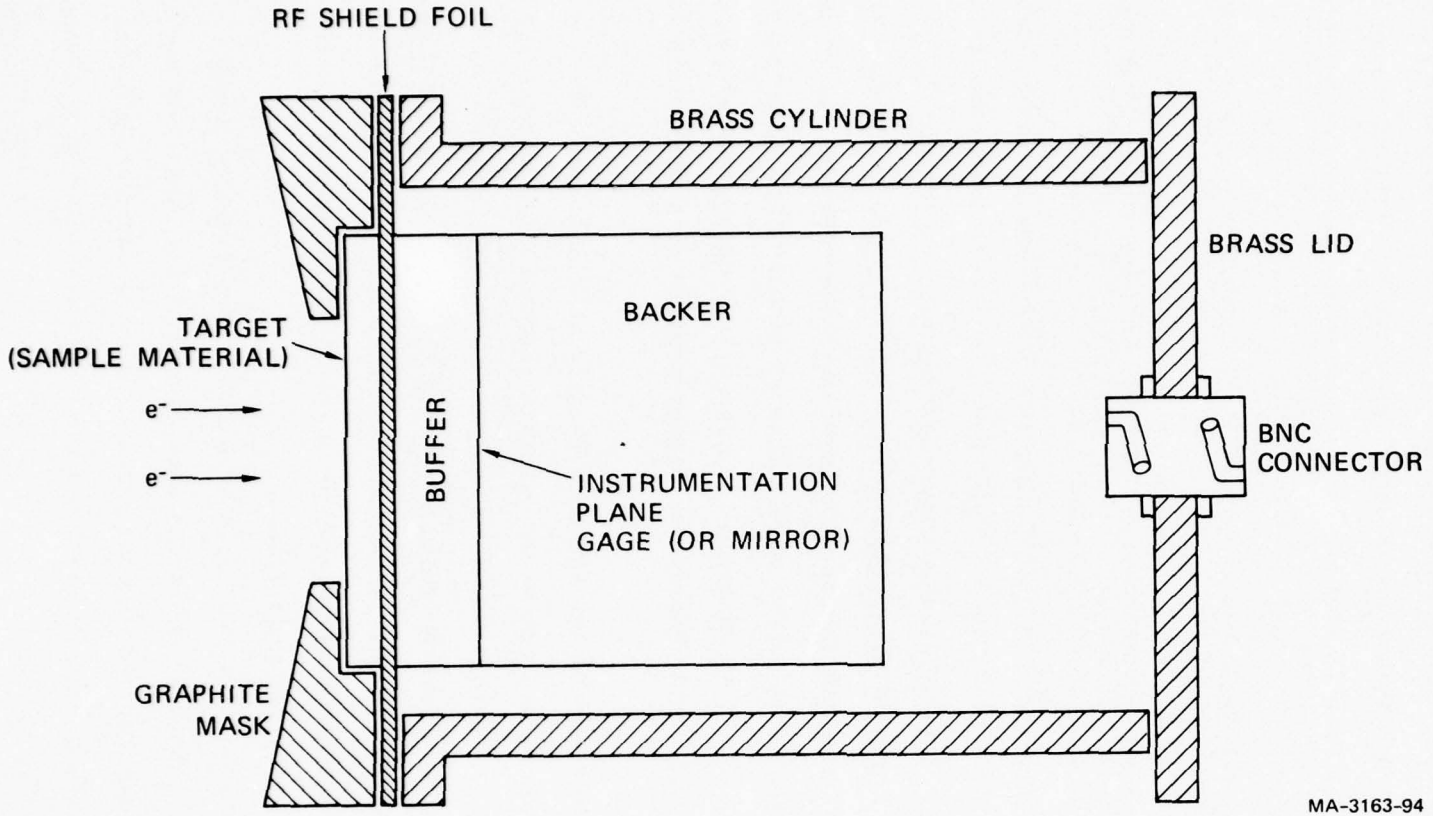


FIGURE 3 RF SHIELDING CANISTER

## D. Summary of Experiments

Table 1 shows the total number of target irradiations, excluding diagnostic shots, performed over approximately five weeks of pulsing on the PI 738 Pulserad.

As noted under "Remarks" in Table 1, not all the attempted shots yielded data usable for material characterization. In the alumina data run (Shots 24402-24433), the four quartz gage shots were too noisy, and Shot 24412 was lost because the beam generator misfired. In the aluminum titanate experiments, seven attempted data shots were of little value. Nine of the PSDB target irradiations were lost.

The first fourteen shots were not intended to give modelling data at all, but were performed to select the best gaging technique and to suppress electrical noise. However, this preliminary sequence yielded two clean traces (Shots 24133 and 24135), which will be reported later among the alumina data (Section III). The usable data are summarized in Table 2 and will be presented in detail in Sections III-V.

Table 1

SHOT DESCRIPTIONS

| Shot | RF-Shield | Buffer | Instrument | Backer | Remarks |
|---|---|---|---|---|---|
| **Sintered Alumina ($Al_2O_3$)** | | | | | |
| 24 126 | 1-mil Al | Glass | Manganin (‖)‡ | Glass | Bad scope camera |
| 24 127 | 1-mil Al | Glass | Manganin (‖)§ | Glass | Noise |
| 24 128 | 1-mil Cu | S-$Al_2O_3$++ | Manganin (⊥) | S-$Al_2O_3$ | Noise |
| 24 129 | 1-mil Cu | S-$Al_2O_3$ | Manganin (⊥) | S-$Al_2O_3$ | Noise |
| 24 130 | 1-mil Cu | S-$Al_2O_3$ | Ytterbium | S-$Al_2O_3$ | Noise |
| 24 131 | 1-mil Cu | S-$Al_2O_3$ | Carbon (⊥) | S-$Al_2O_3$ | Noise |
| 24 132 | 11-mil Al | Glass | Carbon (⊥) | Glass | Noise |
| 24 133 | 5-mil Al | Glass | Carbon (‖) | Glass | Quiet - OK |
| 24 134 | 1-mil Al | Glass | Carbon (‖) | Glass | Misfire |
| 24 135 | 1-mil Al | Glass | Carbon (⊥) | Glass | Fairly Quiet |
| 24 136 | 5-mil Cu | S-$Al_2O_3$ | Manganin (⊥) | S-$Al_2O_3$ | Misfire |
| 24 137 | -- | Al | Carbon (⊥) | Al | Noise |
| 24 138 | 1-mil Al | Glass | Manganin (‖) | Glass | Noise |
| 24 139 | 1-mil Cu | S-$Al_2O_3$ | Ytterbium | S-$Al_2O_3$ | Noise |
| **Sintered Alumina ($Al_2O_3$)** | | | | | |
| 24 402 | 2-mil Cu | S-$Al_2O_3$ | Carbon | S-$Al_2O_3$ | B-1 |
| 24 403 | 2-mil Cu | S-$Al_2O_3$ | Carbon | S-$Al_2O_3$ | B-2 |
| 24 405 | 10-mil Cu | S-$Al_2O_3$ | Carbon | S-$Al_2O_3$ | A-1 |
| 24 406 | 10-mil Cu | S-$Al_2O_3$ | Carbon | S-$Al_2O_3$ | C-1 |
| 24 408 | 2-mil Cu | S-$Al_2O_3$ | Carbon | S-$Al_2O_3$ | D-1 |
| 24 409 | 10-mil Cu | S-$Al_2O_3$ | Carbon | S-$Al_2O_3$ | A-2 |
| 24 412 | 2-mil Cu | S-$Al_2O_3$ | Carbon | S-$Al_2O_3$ | D-2 Misfire |
| 24 424 | 10-mil Cu | S-$Al_2O_3$ | Carbon | S-$Al_2O_3$ | C-2 |
| **Plasma-Sprayed Alumina ($Al_2O_3$)** | | | | | |
| 24 425 | 2-mil Cu | S-$Al_2O_3$ | Carbon | S-$Al_2O_3$ | E-1 |
| 24 428 | 2-mil Cu | S-$Al_2O_3$ | Carbon | S-$Al_2O_3$ | E-2 |
| 24 429 | 2-mil Cu | S-$Al_2O_3$ | Quartz | -- | G-1 Noise |
| 24 430 | -- | Al | Quartz | -- | F-1 Noise |
| 24 432 | -- | Al | Quartz | -- | F-2 Noise |
| 24 433 | 2-mil Cu | S-$Al_2O_3$ | Quartz | -- | G-2 Noise |

Table 1 (Concluded)

SHOT DESCRIPTIONS

| Shot | RF-Shield | Buffer | Instrument | Backer | Remarks |
|---|---|---|---|---|---|
| Aluminum Titanate ($Al_2TiO_5$) | | | | | |
| 24 200 | 2-mil Cu | FQ** | Carbon | FQ | 3-Z |
| 24 201 | 2-mil Cu | FQ | Carbon | FQ | 4-Z Misfire |
| 24 205 | -- | FQ | LDI* & LVI† | FQ | 1-Yu Gap |
| 24 206 | -- | FQ | LDI & LVI | FQ | 2-Yu Gap |
| 24 207 | -- | FQ | LDI & LVI | FQ | 1-Xu Gap |
| 24 212 | -- | FQ | LDI & LVI | FQ | 3-Y |
| 24 213 | -- | FQ | LDI & LVI | FQ | 4-Y |
| 24 215 | -- | FQ | LDI & LVI | FQ | 2XB |
| 24 219 | -- | FQ | LDI & LVI | FQ | 3XB Atypical Beam |
| 24 220 | -- | FQ | LDI & LVI | FQ | 4XB |
| 24 224 | 2-mil Cu | FQ | Ytterbium | FQ | 1-Z Noise |
| 24 225 | 2-mil Cu | FQ | Ytterbium | FQ | 2-Z Noise |
| Plasma-Sprayed Distended Beryllium (PSDB) | | | | | |
| 24 729 | -- | -- | Ytterbium | PSDB | $e^-$-injection into gage |
| 24 730 | -- | -- | Ytterbium | PSDB | $e^-$-injection into gage |
| 24 731 | -- | -- | Carbon | PSDB | $e^-$-injection into gage |
| 24 935 | -- | -- | Carbon | PSDB | SRI-1 Noise |
| 24 940 | -- | -- | Carbon | PSDB | SRI-1 Noise |
| 24 943 | -- | -- | Carbon | PSDB | LLL+ #12-S Noise |
| 24 944 | -- | -- | Carbon | PSDB | LLL #12-S Noise |
| 24 946 | -- | FQ | Carbon | FQ | SRI #4 |
| 24 948 | -- | FQ | Carbon | FQ | SRI #5 |
| 24 949 | -- | FQ | Carbon | FQ | SRI #6 |
| 24 951 | -- | -- | Carbon | PSDB | LLL #10-PS |
| 24 952 | -- | -- | Carbon | PSDB | SRI #3 |
| 24 954 | -- | -- | Carbon | PSDB | LLL #11-PS |
| 24 955 | -- | -- | Carbon | PSDB | LLL #13-S Bad gage |
| 24 959 | -- | FQ | LDI | FQ | SRI #7 Gap |
| 24 960 | -- | FQ | LDI | FQ | SRI #8 |
| 24 963 | -- | FQ | LDI | FQ | SRI #9 |

*LDI = Laser displacement interferometer
†LVI = Laser velocity interferometer
‡ ∥ = Leads parallel to gage plane
§ ⊥ = Leads perpendicular to gage plane
+LLL = Lawrence Livermore Laboratories
**FQ = Fused quartz
++S-$Al_2O_3$ = Sintered alumina

Table 2

USABLE DATA

| Shot | RF-Shield | Buffer | Instrument | Backer | Remarks |
|---|---|---|---|---|---|
| **Sintered Alumina ($Al_2O_3$)** | | | | | |
| 24 133 | 5-mil Al | Glass | Carbon | Glass | Low dose level |
| 24 135 | 1-mil Al | Glass | Carbon | Glass | Low dose level |
| 24 402 | 2-mil Cu | S-$Al_2O_3$ | Carbon | S-$Al_2O_3$ | High dose level |
| 24 403 | 2-mil Cu | S-$Al_2O_3$ | Carbon | S-$Al_2O_3$ | High dose level |
| 24 405 | 10-mil Cu | S-$Al_2O_3$ | Carbon | S-$Al_2O_3$ | High dose level |
| 24 406 | 10-mil Cu | S-$Al_2O_3$ | Carbon | S-$Al_2O_3$ | High dose level |
| 24 408 | 2-mil Cu | S-$Al_2O_3$ | Carbon | S-$Al_2O_3$ | High dose level |
| 24 409 | 10-mil Cu | S-$Al_2O_3$ | Carbon | S-$Al_2O_3$ | High dose level |
| 24 424 | 10-mil Cu | S-$Al_2O_3$ | Carbon | S-$Al_2O_3$ | High dose level |
| **Plasma-Sprayed Alumina** | | | | | |
| 24 425 | 2-mil Cu | S-$Al_2O_3$ | Carbon | S-$Al_2O_3$ | High dose level |
| 24 428 | 2-mil Cu | S-$Al_2O_3$ | Carbon | S-$Al_2O_3$ | High dose level |
| **Aluminum Titanate ($Al_2TiO_5$)** | | | | | |
| 25 200 | 2-mil Cu | FQ | Carbon | FQ | Thick target |
| 25 212 | -- | FQ | LDI & LVI | FQ | Thick target |
| 25 213 | -- | FQ | LDI & LVI | FQ | Thick target |
| 25 215 | -- | FQ | LDI & LVI | FQ | Thin target |
| 25 220 | -- | FQ | LDI & LVI | FQ | Thin target |
| **Plasma-Sprayed Distended Beryllium** | | | | | |
| 24 946 | -- | FQ | Carbon | FQ | Thin target |
| 24 948 | -- | FQ | Carbon | FQ | Thin target |
| 24 949 | -- | FQ | Carbon | FQ | Thin target |
| 24 951 | -- | -- | Carbon | PSDB | Thick target (LLL) |
| 24 952 | -- | -- | Carbon | PSDB | Thick target (SRI) |
| 24 954 | -- | -- | Carbon | PSDB | Thick target (LLL) |
| 24 960 | -- | FQ | LDI | FQ | Thin target |
| 24 963 | -- | FQ | LDI | FQ | Thin target |

## III ALUMINA ELECTRON-BEAM DATA

The originally decreed baseline material for our experiments was sintered alumina, and this material was therefore used for most of our alumina shots. The first two of these shots were conducted at a low dose level (480 ± 60 cal/gm) for the purpose of improving stress gage data collection in severe RF-noise environments. The remainder of the sintered alumina shots were performed at a relatively high dose level (1980 ± 330 cal/gm). Included in the high-dose shots were two plasma-sprayed alumina target shots.

### A. Preliminary Experiments in the Low-Dose Region

The preliminary testing was performed on the PI 738 Pulserad operated at roughly 750 keV mean kinetic energy of the beam pulse. Because of the preliminary nature of these experiments, electron-beam loading was not carefully diagnosed. However, incident fluence was measured with graphite calorimeters indicating a range of 80 ± 10 cal/cm$^2$. A deposition profile, characteristic of this environment, was provided by PI and is shown in Figure 4. Although the depth is indicated in mils of graphite, these profiles are routinely converted to depths in test materials by areal density scaling. The product of the peak normalized dose and the incident fluence measured during the experiments, suggests that the front-surface of the targets was loaded to roughly 480 ± 60 cal/gm.

Table 3 describes the target package geometries of the two stress measurements that were sufficiently noise-free to qualify as data.

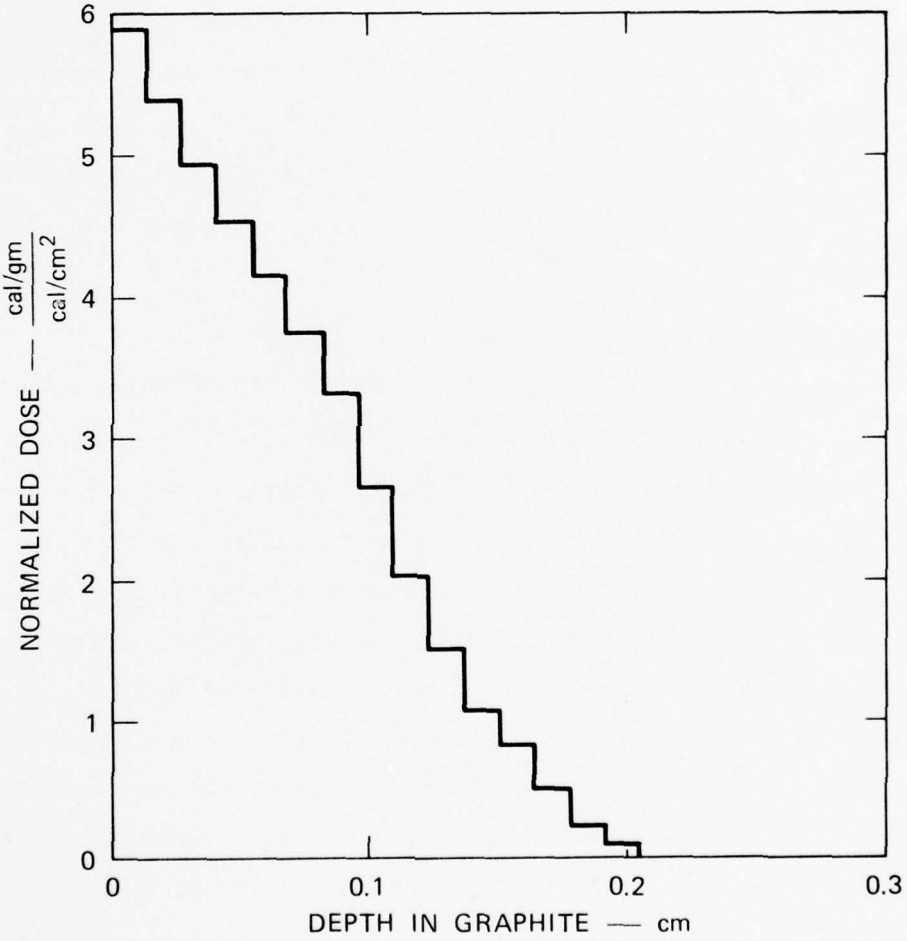


Reference: "Pulsed Electron Beams, Principles and Environments" presented to AFWL by Physics International Co., 23 February 1973.

MA-3163-2A

FIGURE 4 MEASURED DEPOSITION PROFILE IN GRAPHITE FOR PI 738 PULSERAD

Table 3

CONFIGURATION OF LOW-DOSE DATA SHOTS

| Shot | Target Thickness (in.) | RF Shield Thickness (in. Al) | Buffer Thickness (in. glass) | Type Gage | Backer Thickness (in. glass) |
|---|---|---|---|---|---|
| 24133 | 0.050 | 0.005 | 0.060 | Carbon | 0.50 |
| 24135 | 0.050 | 0.001 | 0.060 | Carbon | 0.50 |

One mil of aluminum shielding transmitted a 15-20V noise spike, which interfered slightly with the onset of the stress signal. Five mils of aluminum shielding reduced the RF noise to a 0.6V spike, which went to zero about 200 nsec before onset of the stress signal.

Figure 5 shows the stress history recorded during Shot 24133, and Figure 6 compares the first peaks obtained from Shots 24133 and 24135.

B. Experiments in the High-Dose Region

The RF-noise problem was solved by the combined use of a metallic foil and a time delay between the energy deposition region and the gage. A time delay was introduced by a buffer slab of the test material which postponed stress-wave arrival at the gage until the RF-noise spike, attenuated by the metallic foil, subsided to an amplitude negligible with respect to the deflection produced by the incoming stress pulse.

Data interpretation under these circumstances is simplified by minimizing the thickness of both foil and buffer, but the severity of the noise environment limits that reduction. The stress-wave propagation time between the energy deposition region and the gage can be shortened only with a thicker RF foil; conversely, if the RF foil must be kept thin, then the buffer thickness (propagation delay) must be made large, but not so large as to allow radial stress-relief to reach the gage before the axially propagating stress pulse has passed through the gage plane.

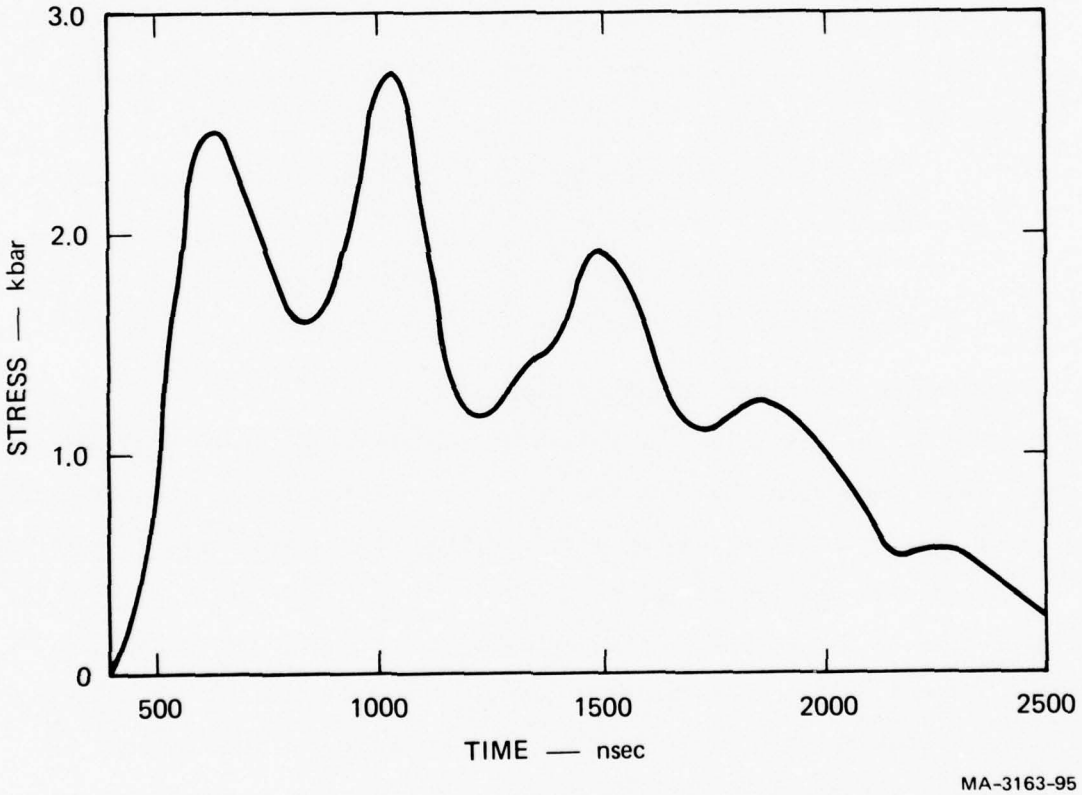


FIGURE 5 STRESS HISTORY FOR SHOT 24133

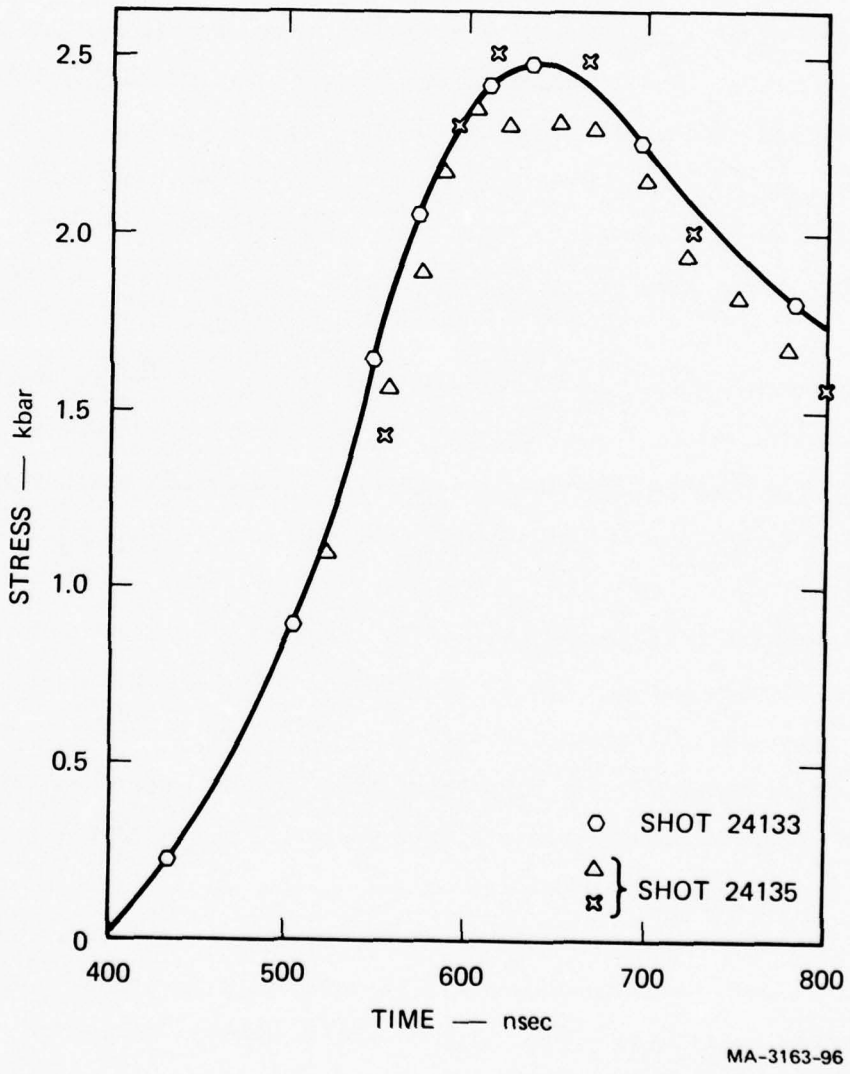


FIGURE 6 FIRST COMPRESSIVE PEAK

The goals of the alumina experiments were to load the test material to the highest dose levels available on the PI 738 Pulserad (consistent with spot sizes giving suitable I-D read-times) and then to record the generated stress waves after propagating them through several different thicknesses of cold (unirradiated) test material.

Sintered alumina is heavily represented in the configurations described in Table 4. All target slabs, except those of configuration D, have the same thickness. The target slab thicknesses were chosen to stop the highest energy electrons in the anticipated beam pulse. The targer slabs were bonded to 2-mil or 10-mil-thick copper foils (RF shields) which were, in turn, bonded to buffers 50, 150, or 300 mils thick--the intended variables in these experiments.

Configuration A has the thinnest buffer and hence, the thickest RF foil. Configuration C has the same RF foil as A but propagates the stress wave through unirradiated material three times thicker than that of A. The RF foil is the sole variable between Configurations B and C.

Configuration D is the inverse of B. In both cases, the amount of sintered alumina between the target front surface and the gage is the same. The only difference between D and B is the location of the RF foil. The impetus for the D-configuration was our desire to withdraw the ground plane two additional electron ranges deeper into the (dielectric) material, to allow us to record the effect of the worst possible charge buildup. One of the configuration D shots did show a late arriving pulse with reduced amplitude, as could be expected from change buildup effects. This qualitative observation confirms the use of the RF foil as a charge drain. Unfortunately, a replication of this shot failed because of machine prefire.

The target slabs of the E-configuration are plasma-sprayed alumina, although the buffers are sintered.

Table 4: ALUMINA DATA

| Shot | Configuration | Target Material | Target Thickness (mils) | Copper Thickness (mils) | Sintered Alumina Buffer Thickness (mils) | Dose, D, in cal/gm, versus Depth, x, in cm Target Material |
|---|---|---|---|---|---|---|
| 25405 | A-1 | Sintered Alumina | 52.5 | 10.3 | 54.0 | $D(cal/gm) = 1830 \exp\{-14.56x\} \cos 14.56x$ |
| 25409 | A-2 | Sintered Alumina | 52.c | 10.3 | 52.8 | $D(cal/gm) = 2020 \exp\{-16.39x\} \cos 16.39x$ |
| 25402 | B-1 | Sintered Alumina | 53.2 | 2.2 | 147.8 | $D(cal/gm) = 1820 \exp\{-14.40x\} \cos 14.40x$ |
| 25403 | B-2 | Sintered Alumina | 52.7 | 2.2 | 146.8 | $D(cal/gm) = 1650 \exp\{-12.89x\} \cos 12.89x$ |
| 25406 | C-1 | Sintered Alumina | 52.7 | 10.3 | 148.5 | $D(cal/gm) = 1850 \exp\{-14.67x\} \cos 14.67x$ |
| 25424 | C-2 | Sintered Alumina | 52.7 | 10.3 | 145.2 | $D(cal/gm) = 1940 \exp\{-15.57x\} \cos 15.57x$ |
| 25408 | D-1 | Sintered Alumina | 148.5 | 2.2 | 54.5 | $D(cal/gm) = 2100 \exp\{-17.15x\} \cos 17.15x$ |
| 25425 | E-1 | Plasma-Sprayed Alumina | 56.4 | 2.2 | 277.2 | $D(cal/gm) = 2180 \exp\{-15.88x\} \cos 15.88x$ |
| 25428 | E-2 | Plasma-Sprayed Alumina | 56.4 | 2.2 | 277.3 | $D(cal/gm) = 2310 \exp\{-17.21x\} \cos 17.21x$ |

The analytical expressions of energy deposition profiles of Table 4 were derived from a large body of transmitted fluence measurements. These expressions are capable of tracking modest shot-to-shot variations in peak accelerating voltage using a method described in References 1 and 3.

Figures 7-11 show the carbon gage records for configuration A-E, as listed in Table 4.

---

[3] A. Lutze, "Empirically Fit Deposition Profiles Reflecting Dependence on Accelerating Voltage" (in preparation).

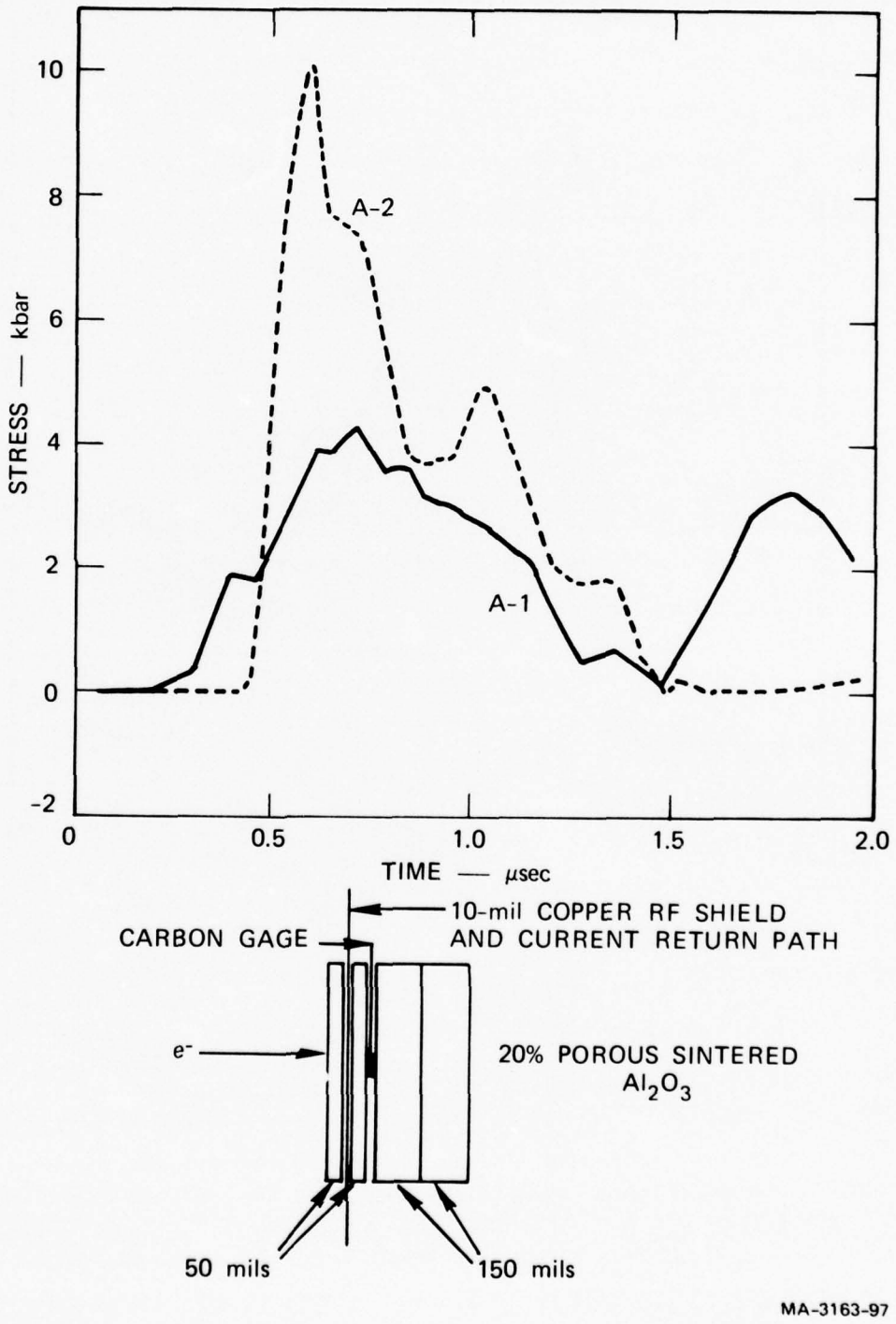


FIGURE 7 CARBON GAGE RECORD—CONFIGURATIONS A-1 AND A-2 (TABLE 4)

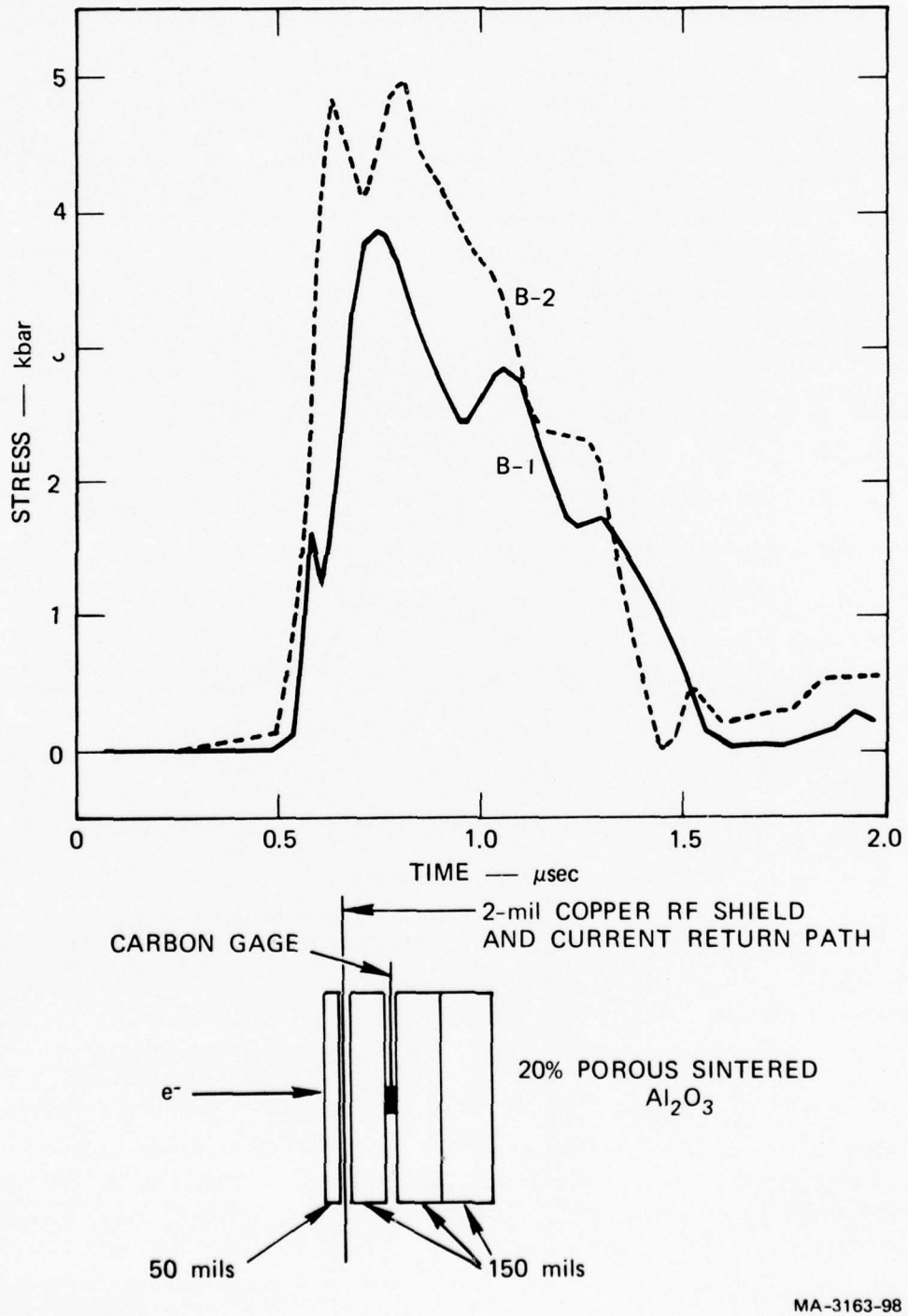


FIGURE 8 CARBON GAGE RECORD—CONFIGURATIONS B-1 AND B-2 (TABLE 4)

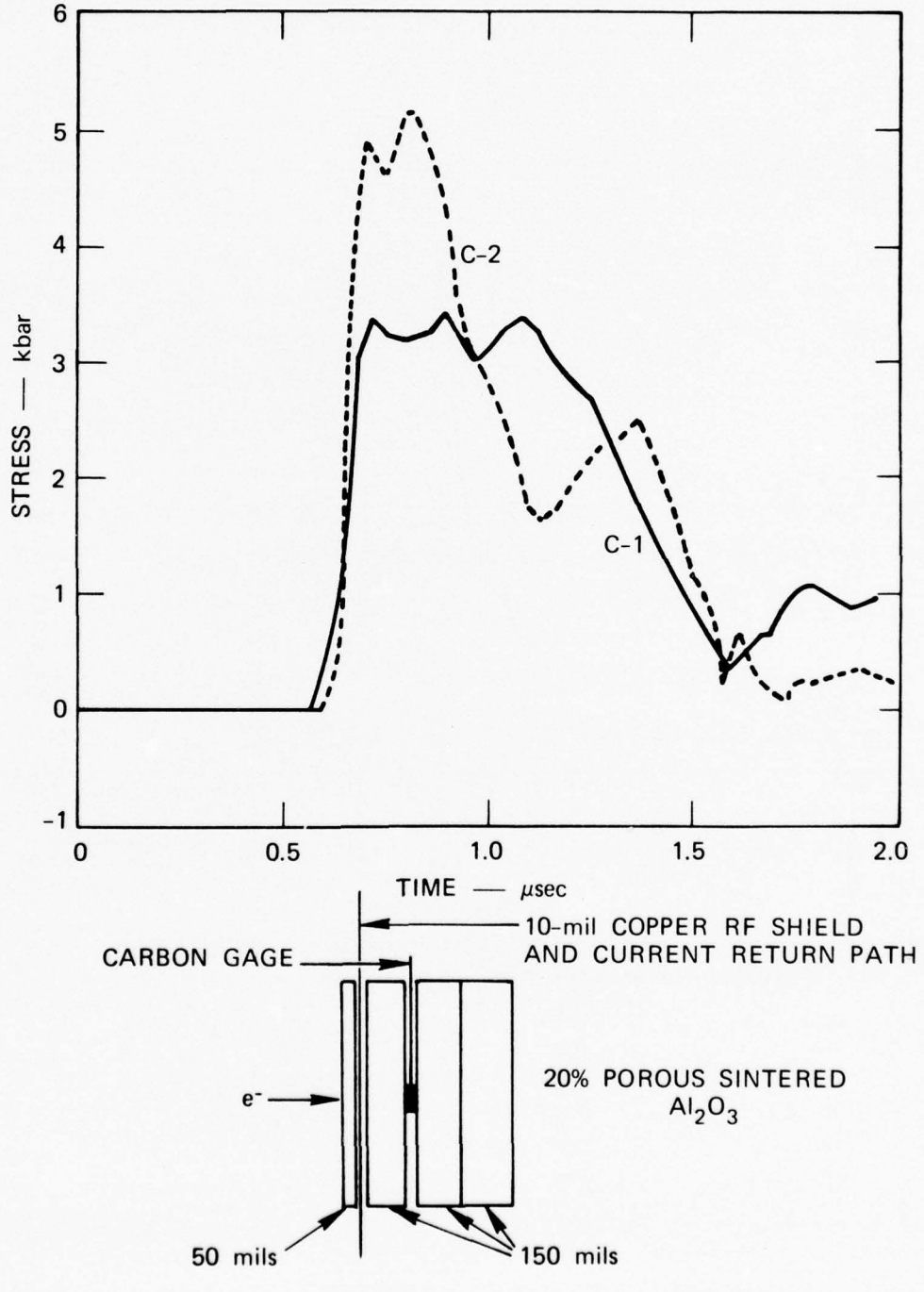


FIGURE 9 CARBON GAGE RECORD—CONFIGURATIONS C-1 AND C-2 (TABLE 4)

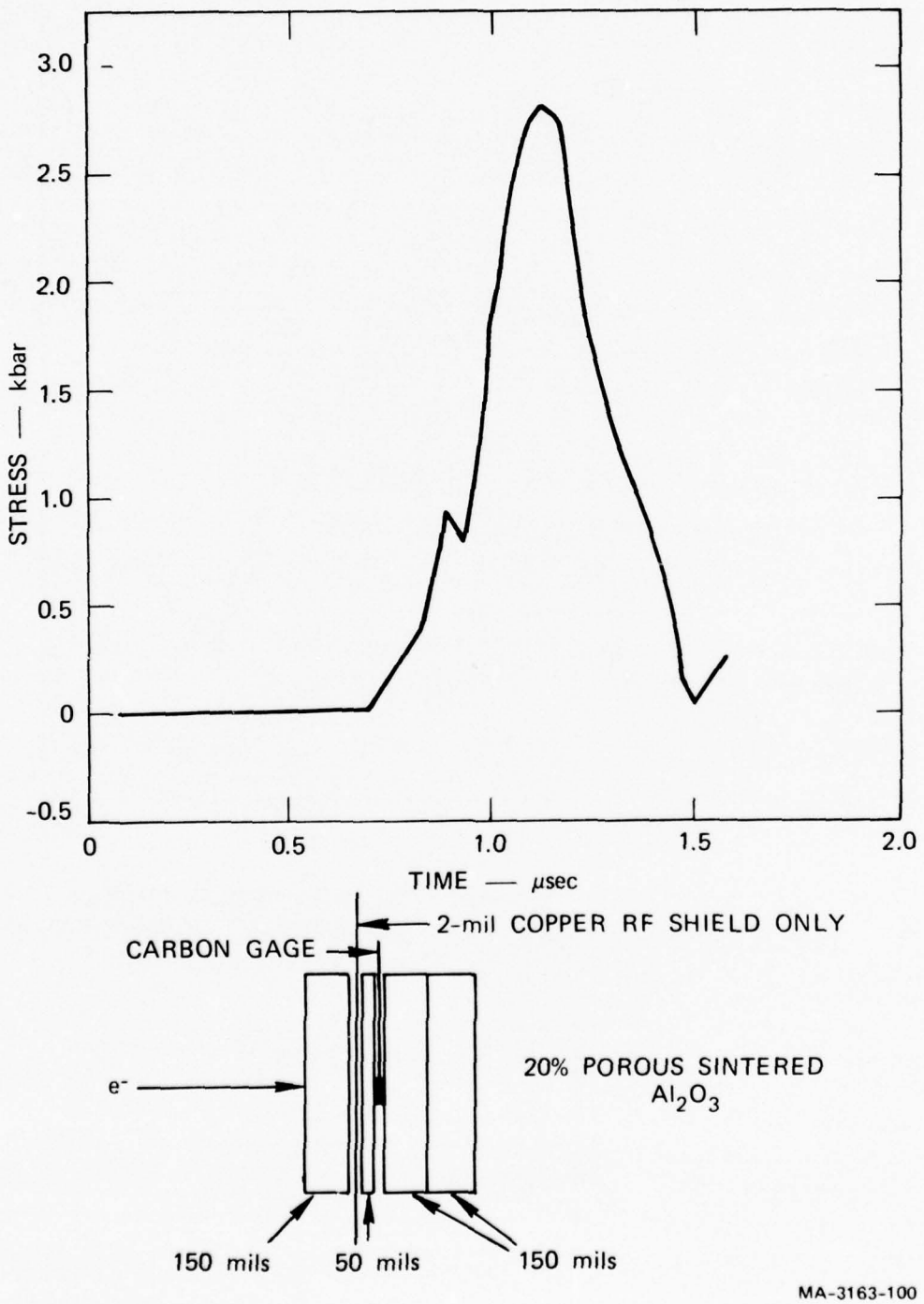


FIGURE 10 CARBON GAGE RECORD—CONFIGURATION D-1 (TABLE 4)

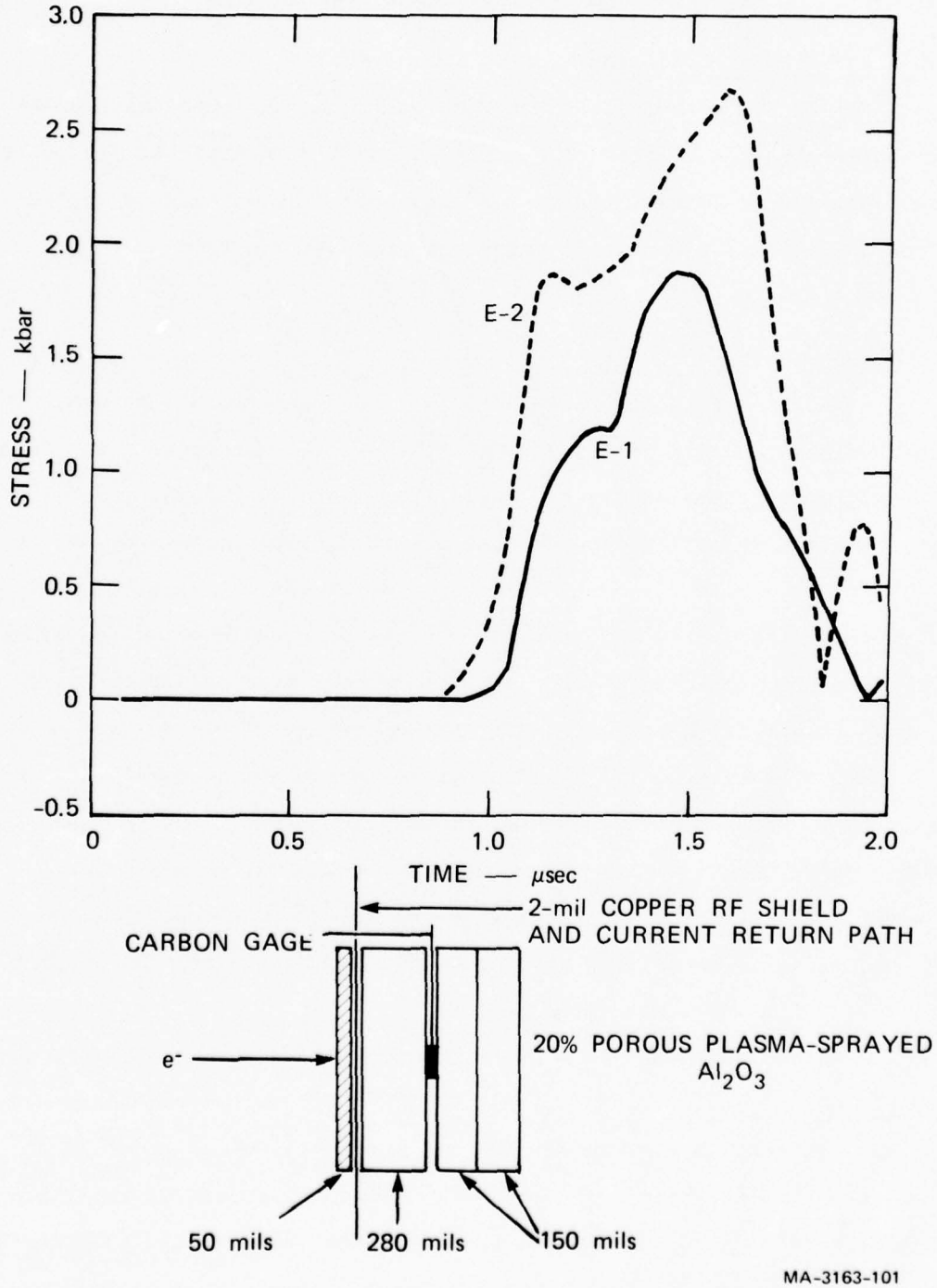


FIGURE 11 CARBON GAGE RECORD—CONFIGURATIONS E-1 AND E-2 (TABLE 4)

## IV ALUMINUM TITANATE ELECTRON-BEAM DATA

### A. Irradiation Conditions

The PI 738 Pulserad was used as the source of approximately 700 keV mean electron energy. The energy deposition profile in Figure 12 was obtained by transmitted fluence measurements, which were scaled from graphite (1.8 gm/cm$^3$) to aluminum titanate ($Al_2TiO_5$) (3.4 gm/cm$^3$) by areal density.

### B. Response Measurements

Laser interferometry was the main instrumentation technique. The displacement and the velocity modes were used simultaneously to simplify data interpretation and to safeguard against loss of information should the particle velocities be too fast for the displacement mode or too slow for the velocity mode. The delay leg in the velocity mode was adjusted to provide as much overlap between the two modes as possible. We began the data collection with a few stress gage measurements to confirm laser interferometer setup parameters.

The objective of the target package design was to make measurements as near as possible to the energy deposition region. The package design was complicated by electron penetration through the porous target material in excess of areal density scaling expectations with injection of excessive currents into gage circuits, and by the need for a good mirror for interferometric measurements.

A mirror could not be vapor-deposited onto a porous surface, so we bonded the range-thick (approximately 60 mil) aluminum titanate targets to thin (approximately 20 mil) fused silica buffers. The instrumentation plane (gage or mirror) was then located in the fused silica between the thin buffers and the thick (approximately 250 mil) backers. To shield the stress gages in the target packages from R-F noise, we put a 2-mil copper foil at the target-buffer interfaces.

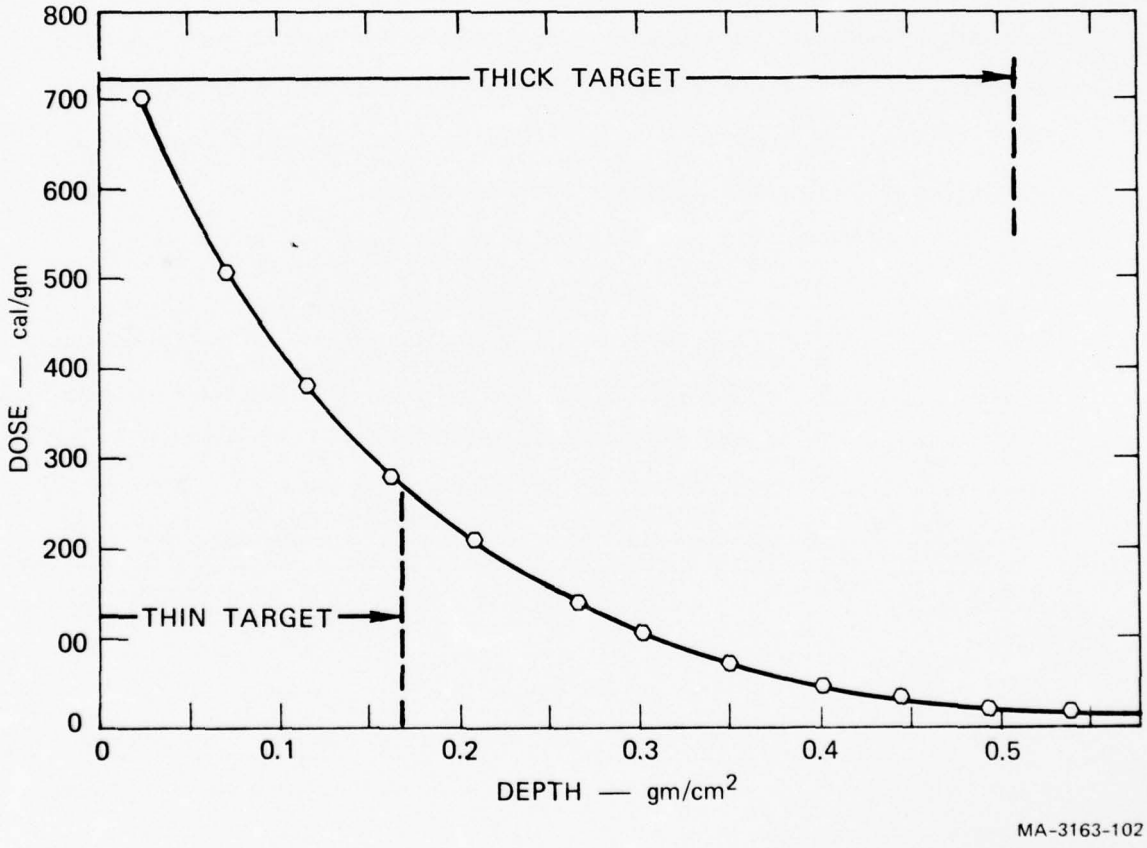


FIGURE 12 ENERGY DEPOSITION PROFILE FOR ALUMINUM TITANATE EXPERIMENTS

Eight target packages were prepared for irradiation: two with carbon gages, two with ytterbium gages, and four with mirrors vapor-deposited onto the backer surfaces for interferometric measurements.

The two ytterbium gage records were overwhelmed by electrical noise, and one of the carbon gage measurements was lost because of improper pretriggering of the gage power supply. The only gage trace obtained, Figure 13, is weakened by a large noise signal just preceding the stress pulse. The purpose of this measurement was to study peak stress arrival and amplitude to take the best advantage of available oscilloscopes in displaying laser interferograms.

Figure 14 shows the particle velocity profiles in fused silica for three of the four target packages prepared for laser interferometric measurements. One of the four, not shown in Figure 14, yielded no data within the time of observation--probably because of a substantial gap between target and buffer. Shot 25205, in Figure 14, shows the effect of a lesser gap. After Shot 25205, the remaining target packages were disassembled and rebonded. The results are seen in the profiles for Shots 25212 and 25213; the latter appears affected by reduced machine output.

Examination of machine-output monitors suggests that Shot 25212 is the response to energy deposition shown in Figure 12 for the thicker target configuration. Figure 15 shows the data obtained on Shot 25212. Aside from the absence of a 2-mil copper foil, the target configuration is identical to that of the carbon gage record shown in Figure 13. The particle velocity profile for Shot 25212 was obtained from simultaneous displacement and velocity interferometer measurements. In Figure 15, circles represent data from oscilloscopes run at 20 nsec/cm, while crosses give data from a 50 nsec/cm oscilloscope--the last in a cascading oscilloscope array.

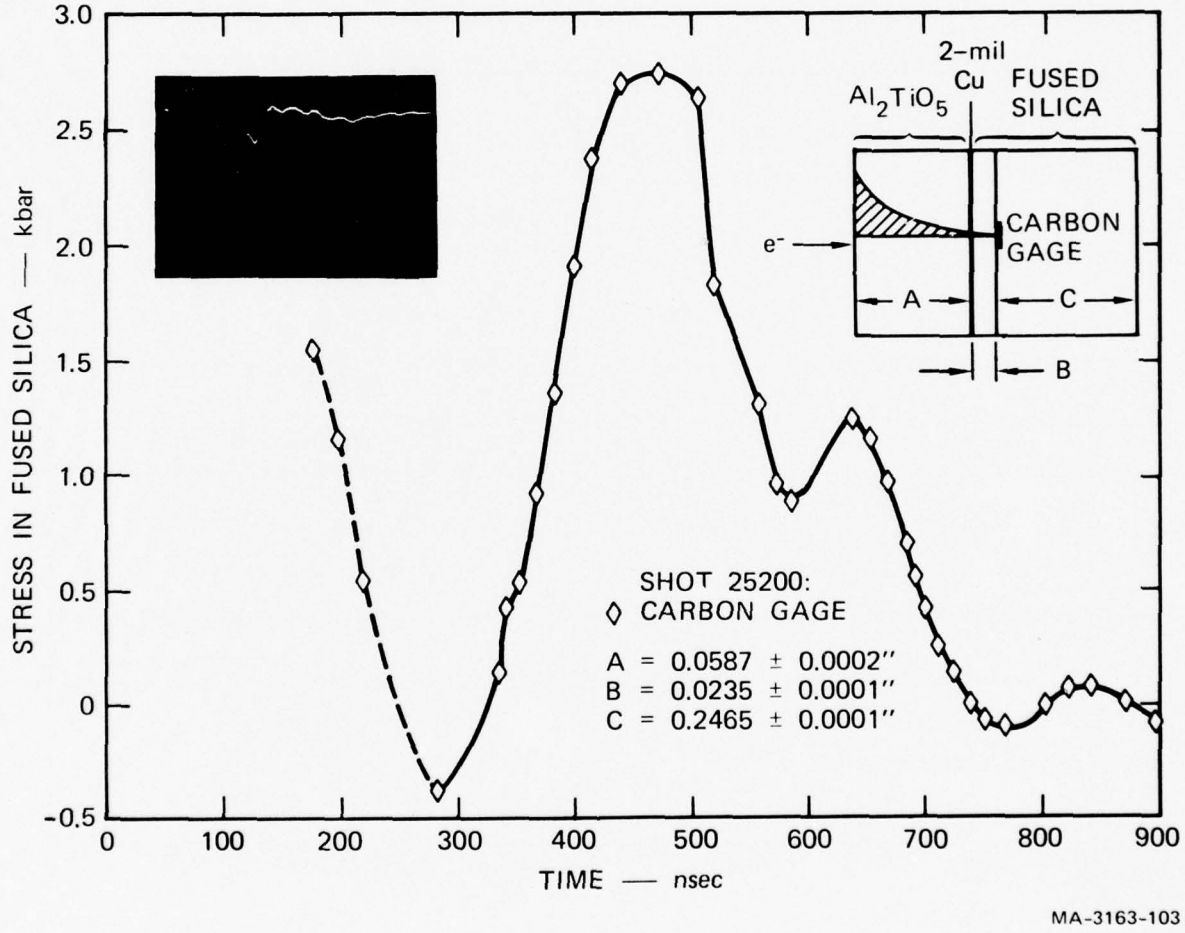


FIGURE 13 CARBON GAGE RECORD FOR SHOT 25200

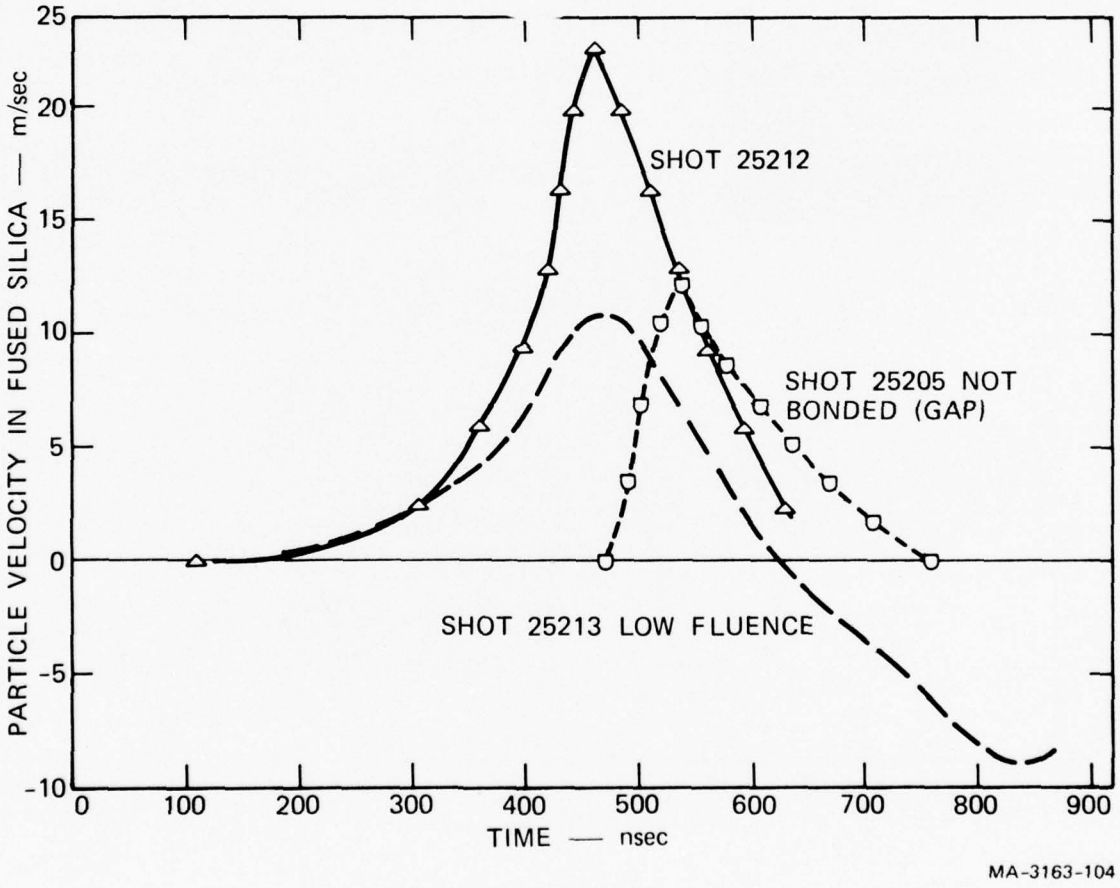


FIGURE 14 ALUMINUM TITANATE "THICK TARGET" PARTICLE VELOCITY PROFILES

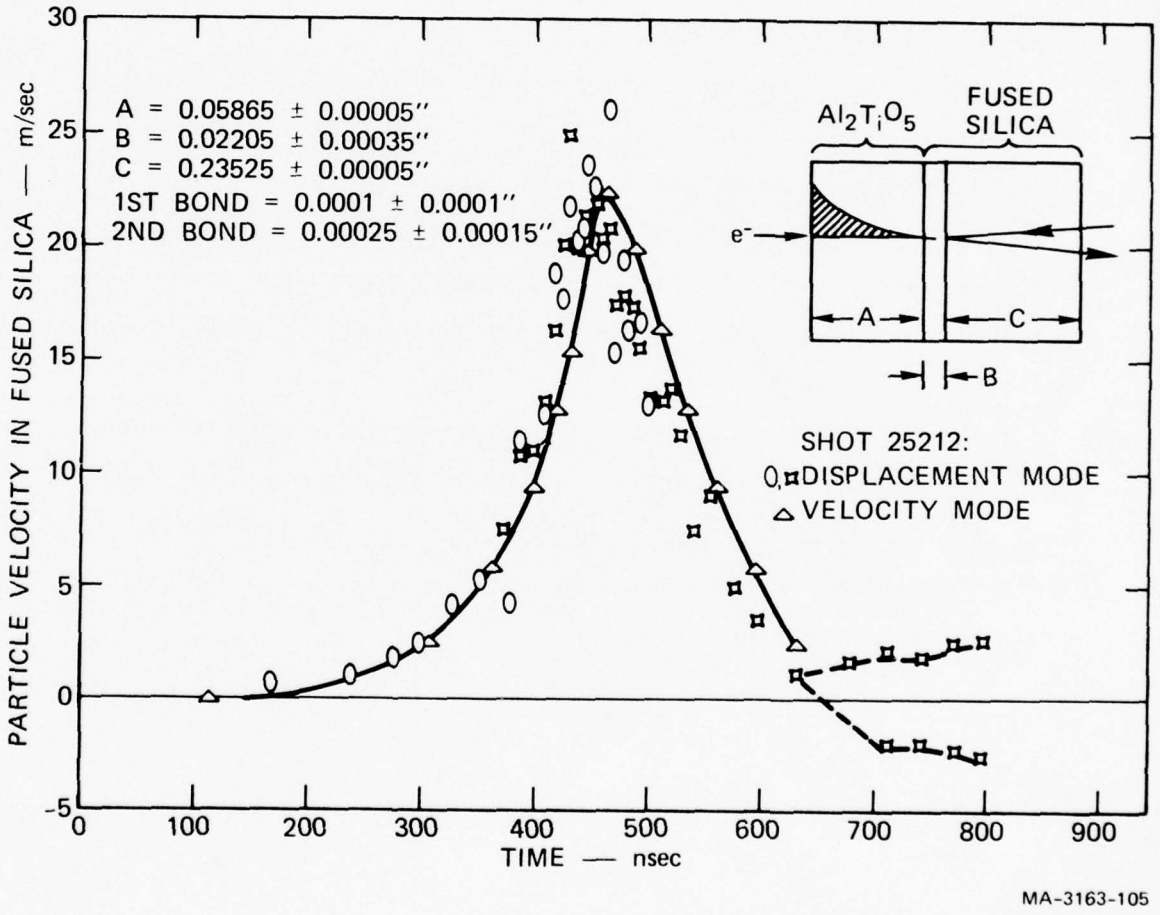


FIGURE 15 PARTICLE VELOCITY PROFILE FOR SHOT 25212

The "thick-target" design prevented energy deposition in bonds but necessitated measurements outside the energy deposition region. We also assembled four target packages in which the target was less than range thick (approximately 20 mils hafnium titanate). The target was pressed against the fused silica buffer and bonded only peripherally (no bond at the interface).

Irradiation of the first two unbonded, thin targets yielded no data, and on close examination of the irradiated target packages, we found that the peripheral bond had crept in at the edges between target and buffer, thereby separating them. We decided to disassemble the remaining two thin targets and to bond the dry interfaces in the hope that a thin enough bond in the energy deposition region would be either "modelable" or negligible.

Figure 16 shows the bonded, thin-target particle velocity data from simultaneous measurements in the displacement and the velocity modes during Shot 25220. Figure 17 compares the results from the irradiations of the two bonded, thin targets--Shots 25215 (velocity mode only) and Shot 25220.

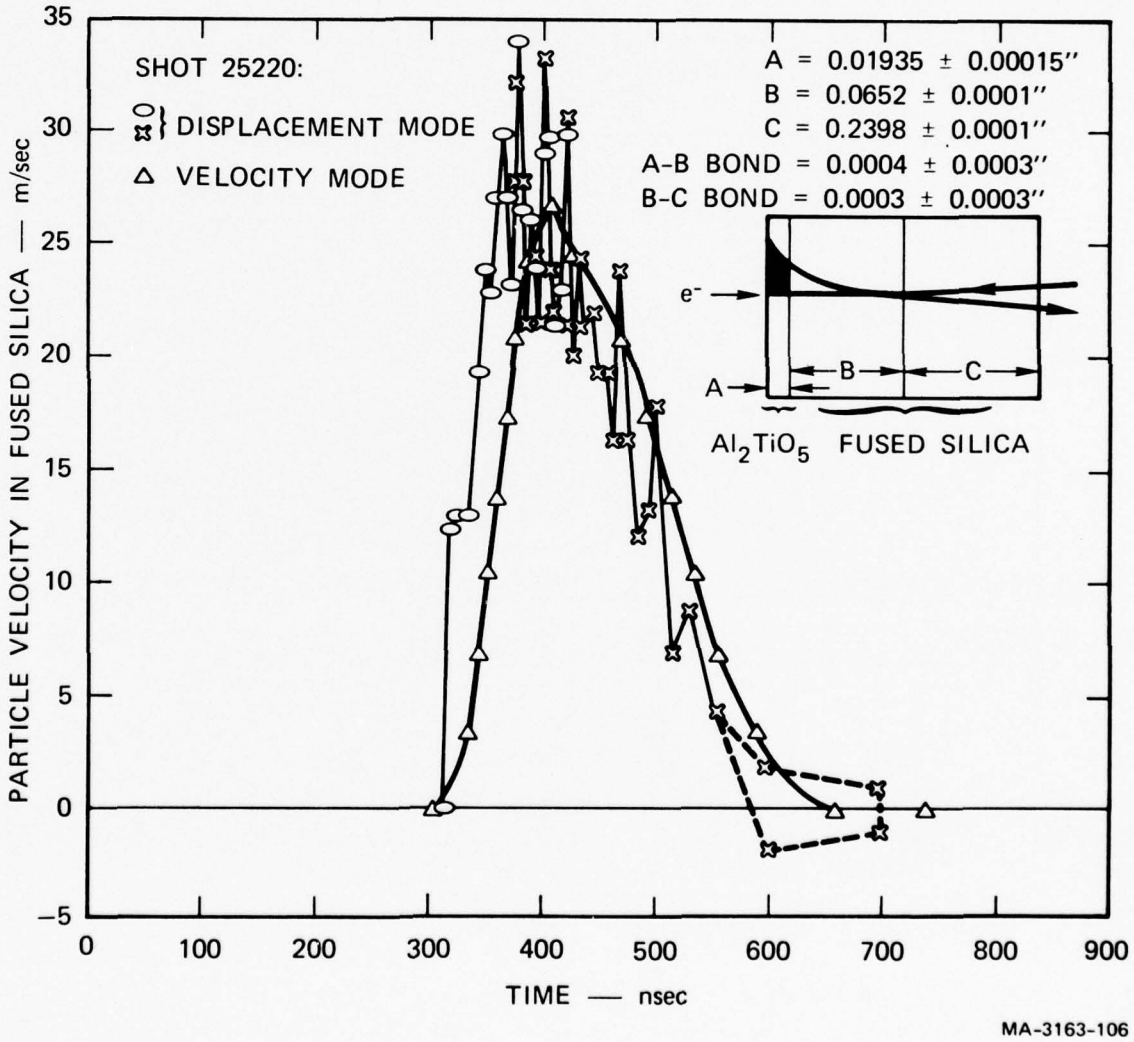


FIGURE 16 PARTICLE VELOCITY PROFILE FOR SHOT 25220

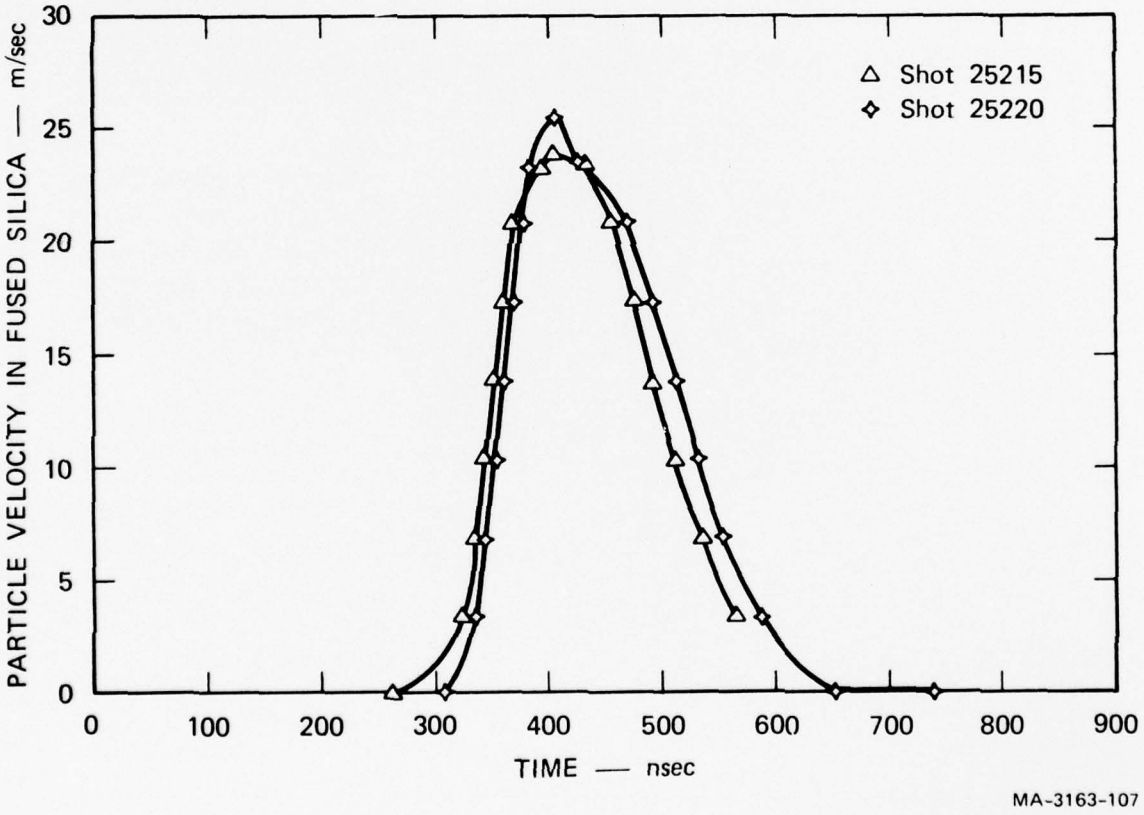


FIGURE 17 ALUMINUM TITANATE "THIN TARGET" PARTICLE VELOCITY PROFILES

# V BERYLLIUM ELECTRON-BEAM DATA

The PI 738 Pulserad was used to measure stress profiles generated in beryllium by electron beam irradiation at peak dose levels below its melt energy. These experiments were performed to observe the effect of pore compaction in the heated region (below melt).

The beryllium targets were assembled in two configurations: in-material and quartz-backed. The in-material configurations consisted of a carbon gage bonded between two 200-mil-thick slabs of porous beryllium. The first slab served as the target; the second, as the backer.

In the quartz-backed configuration, 100-mil porous beryllium targets were butted against and peripherally potted to 63-mil fused quartz buffers. A carbon gage was then bonded between the buffer and a 0.25-inch fused quartz backer slab. Quartz-backed configurations were also fabricated for laser interferometer recording of particle velocities. An aluminum mirror was vapor-deposited onto the rear surface of the 63-mil buffer, which was then bonded to the 0.25-inch backer. The carbon gage and the interferometer packages contained no bond at the interface between target and fused-quartz buffer, since that interface was intended to be in the energy deposition region. This arrangement was motivated by a desire to capture the stress wave (emerging from the heated region of PSDB) in some well-characterized, elastic material, thereby preventing stress propagation through both heated and cold, porous beryllium; we gambled that the beryllium targets could be butted against the fused-quartz buffers in acoustic contact, that is, constructed without a gap between them.

In addition to the SRI baseline test material (PSDB), two materials, plasma-sprayed and sintered beryllium, were supplied by LLL. These materials were instrumented at SRI and are included in the experiments reported here. Table 5 summarizes these materials and their test configurations.

Table 5

TEST MATERIALS AND INSTRUMENTATION CONFIGURATIONS

| Target Material | Configurations | | |
|---|---|---|---|
| | In-material (carbon gage) | Quartz-backed (carbon gage) | Quartz-backed (interferometer) |
| SRI PSDB | 3 | 3 | 3 |
| LLL plasma-sprayed beryllium | 2 | - | - |
| LLL sintered beryllium | 2 | - | - |

Note: LLL was limited to a total of four shots but was given a choice of selecting target configurations.

A. Response Measurements

Figures 18-21 give the material response data representing combinations of two packaging and two instrumentation techniques.

Figure 18 shows the results of two laser-interferometer measurements in the displacement mode. Discrete points in Figure 18 are average velocities computed from half-fringe displacements (0.122 μm) over the time duration between them. The interferometer output was displayed on six cascaded (overlapping) oscilloscopes, each operated at 50 nsec/cm and giving better than 10 nsec time-resolution. The difference between the two particle velocity profiles is most likely attributable to shot-to-shot variations in electron-beam irradiation conditions.

Figure 19 displays two carbon gage measurements in the quartz-backed configurations. In both cases, the loading calibration was used to reduce the unloading portion of the profile. The more appropriate unloading calibration can be used whenever one becomes available. Carbon gages were approximately 60 mils (of fused quartz) away from the energy deposition region; that is, no energy was directly deposited in the gage.

Experiments reported here included four stress measurements with two types of beryllium targets provided by LLL and instrumented with carbon gages (in-material configuration) at SRI. Figure 20 displays stress histories measured in the plasma-sprayed LLL targets, which were similar to PSDB in density and method of preparation, unlike the sintered version. Shot 24 951 in Figure 20 (dotted line) may have received a stress contribution from a thin layer of conducting paint. Posttest inspection of that target showed traces of conducting paint (used to improve grounding for noise suppression) on the target front surface. The paint applied at the target periphery apparently was not sufficiently dry and ran across the front surface during pump-down when the target was in a vertical position. Subsequent targets were allowed to dry thoroughly before irradiation and showed no evidence of paint on front surfaces. None of the interferometer shots required paint grounding.

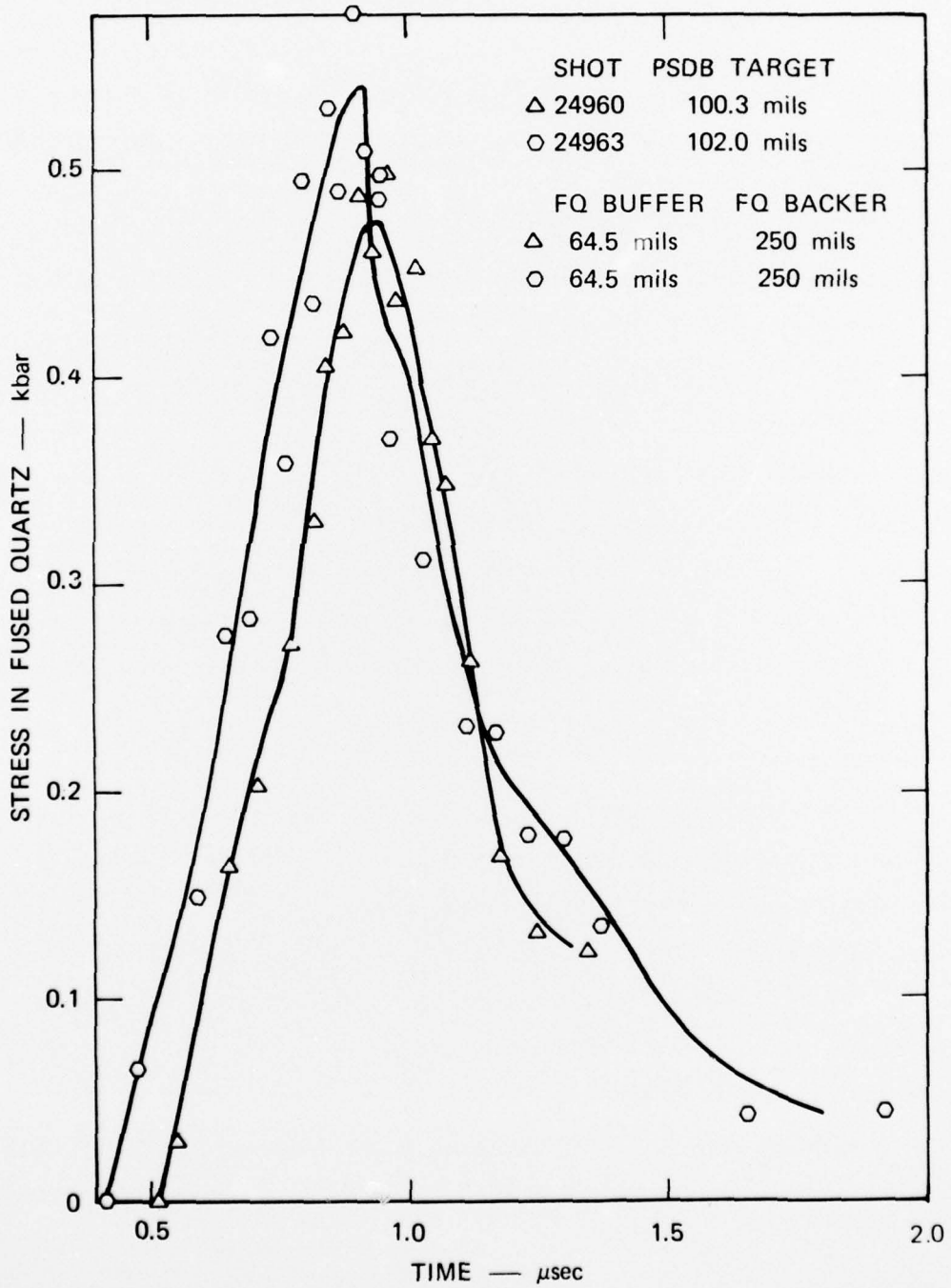


FIGURE 18 LASER INTERFEROMETER RECORD, PSDB, QUARTZ-BACKED

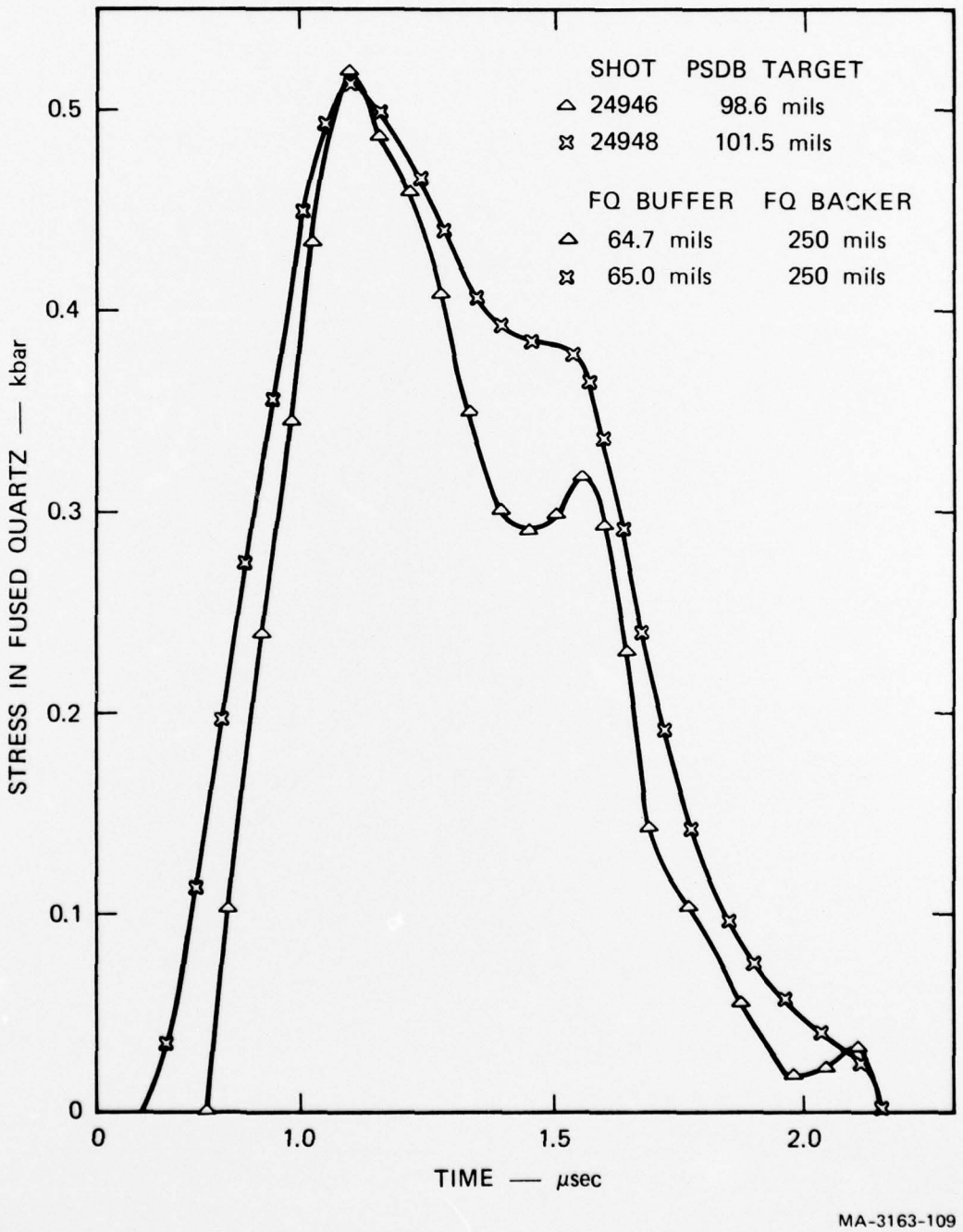


FIGURE 19 CARBON GAGE RECORD, PSDB, QUARTZ-BACKED

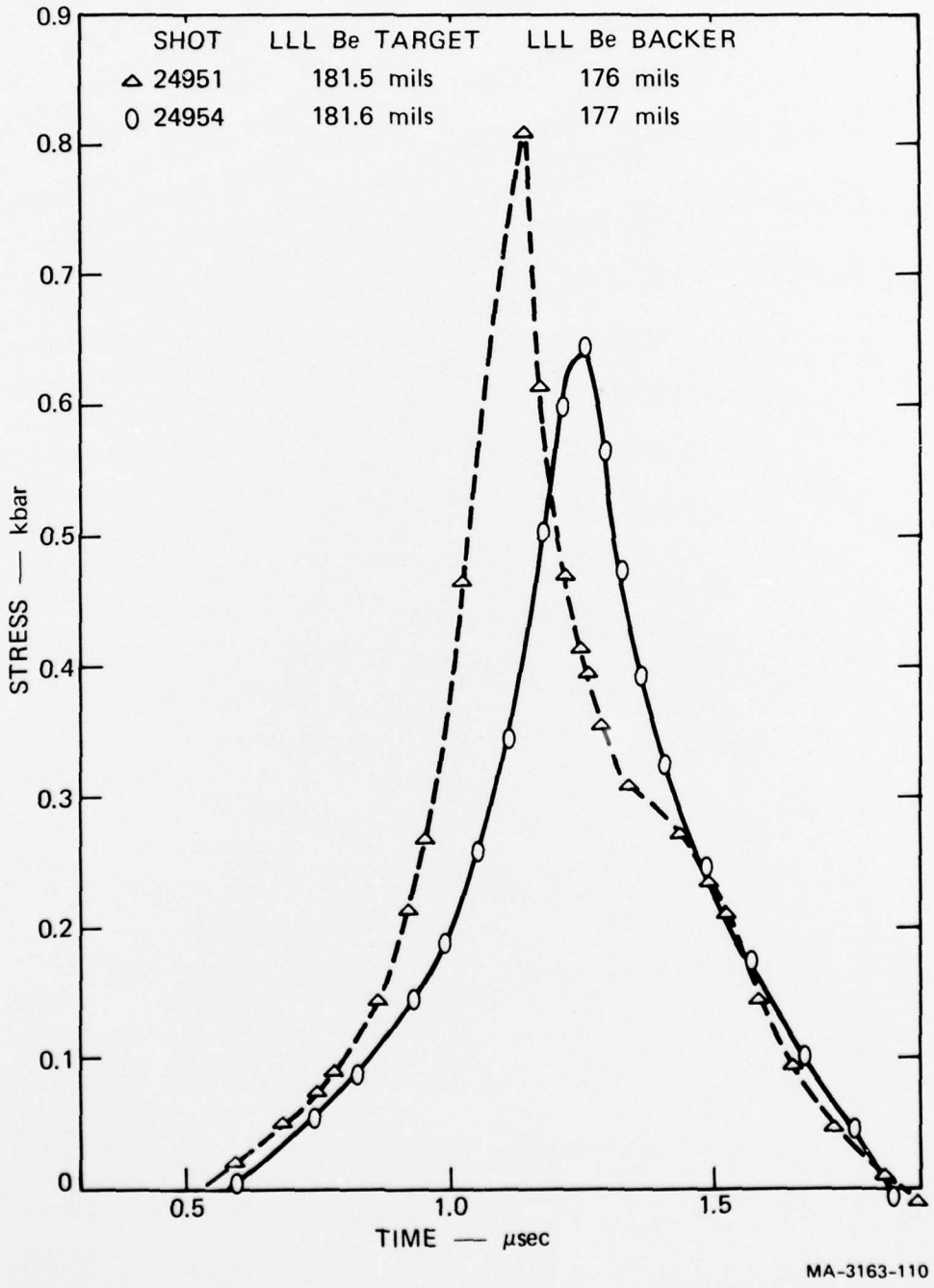


FIGURE 20 CARBON GAGE RECORD, LLL PLASMA-SPRAYED BERYLLIUM, IN-MATERIAL

Three carbon gage measurements were attempted with the in-material configuration in PSDB. Two of these yielded no records, Shot 24935 was too noisy, and the other package suffered a poor electrical contact in the gage. Figure 21 shows Shot 24952 compared with the LLL plasma-sprayed data from Shot 24954.

## B. Irradiation Conditions

In diagnosing electron beam conditions our approach was to identify a radiation environment that was common to some of the response data shots as well as adequately represented among the diagnostic shots. We used transmitted fluence measurements to define a normalized energy deposition profile and an incident fluence representing the loading conditions for some of the response data. Replication shots were performed to increase the probability of finding data with similar radiation loading and to indicate the extent to which beam nonrepeatability was reflected in the response data.

Figure 22 displays the normalized deposition profile and the incident fluence, obtained as described above, and identifies the response data shots for which these loading conditions apply.

## C. Comparison and Evaluation of Results

The response data reported here consist of permutations of two packaging and two instrumentation techniques. In particular,

(1) Range-thick PSDB quartz-backed particle velocity measurements in fused quartz.

(2) Range-thick PSDB quartz-backed stress measurements in fused quartz.

(3) In-material stress measurements preceded by twice-range-thick PSDB.

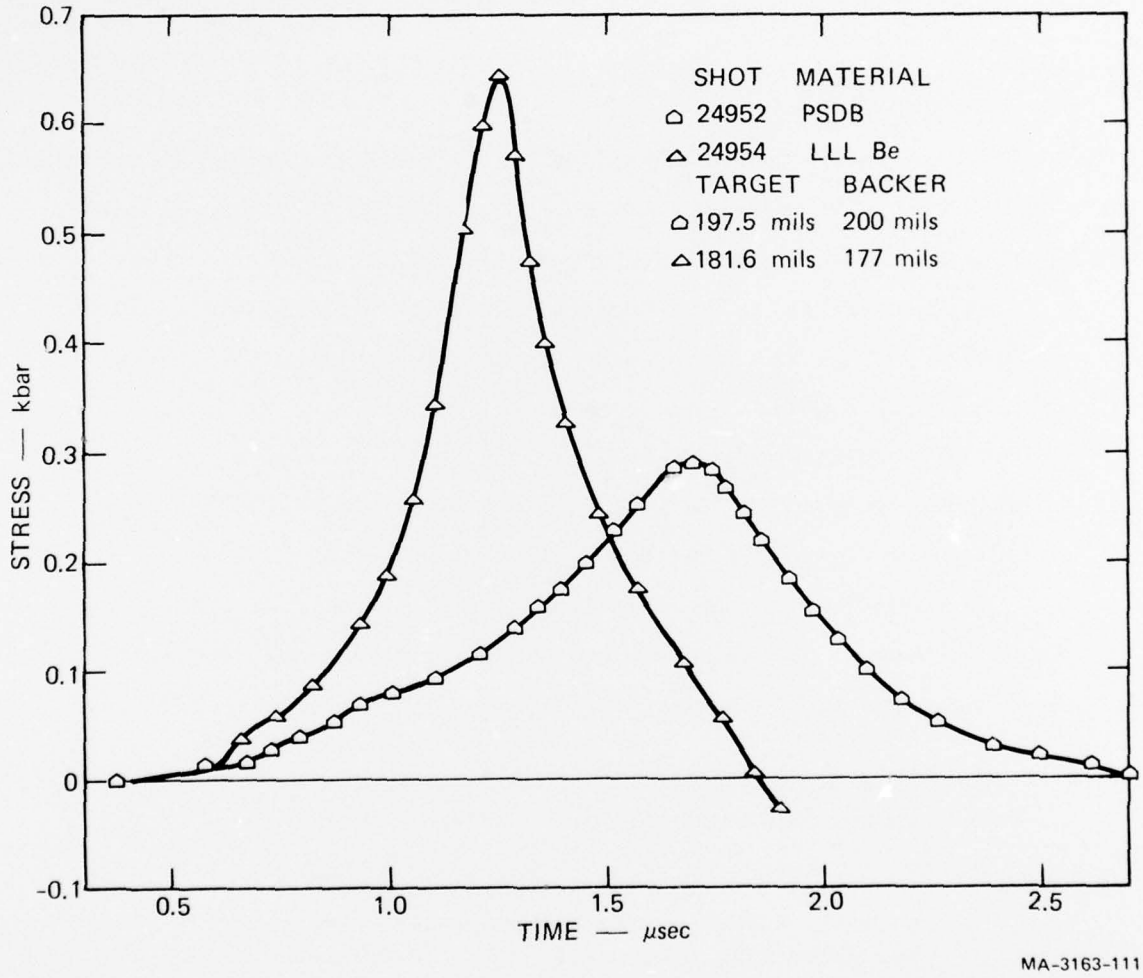


FIGURE 21 CARBON GAGE DATA, LLL PLASMA-SPRAYED BERYLLIUM AND PSDB, IN-MATERIAL

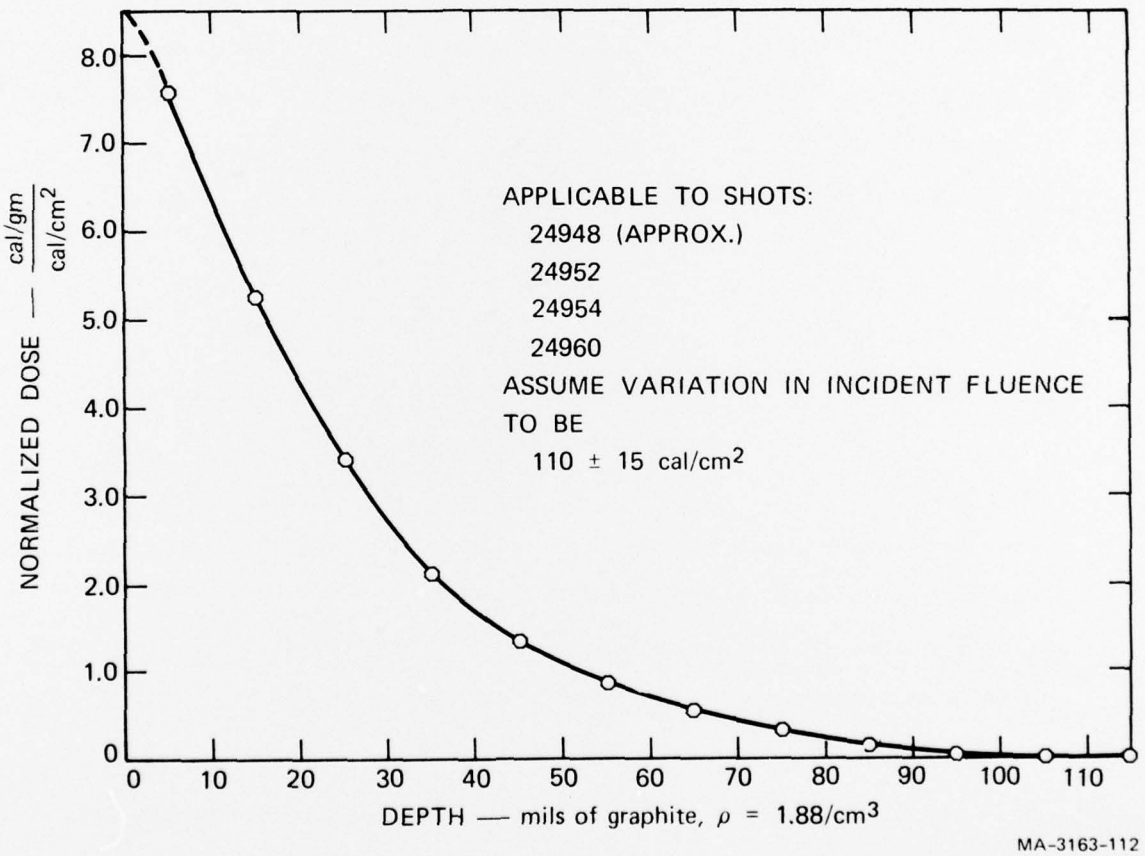


FIGURE 22 ELECTRON LOADING CONDITIONS

The extent of nonrepeatability in the beam conditions appears to be quite reasonable considering replications of each configuration separately (Figures 18, 19, and even 20). The error in grouping the four data shots in Figure 22 by similarity in voltage and current traces must be less than the effect of overall beam nonrepeatability evidenced by response variations within a data pair (the same packaging and instrumentation technique).

Comparison of Figures 18 and 19 shows a significant difference between the interferometer and the carbon gage responses. The comparison can be somewhat quantified by considering two shots with similar beam loading condition. Table 6 shows some parameters useful in the comparison.

Table 6

COMPARISON OF INTERFEROMETER AND CARBON GAGE DATA UNDER IDENTICAL PACKAGING AND SIMILAR IRRADIATION CONDITIONS

| | Interferometer | Carbon Gage |
|---|---|---|
| Shot No. | 24960 | 24948 |
| Arrival of peak stress (μsec) | 0.95 | 1.10 |
| Peak stress in fused quartz (kbar) | 0.48 | 0.53 |
| Rise time from 10% of peak (μsec) | 0.38 | 0.35 |
| Width at half-maximum (μsec) | 0.39 | 0.77 |

The two measuring techniques agree rather well during the loading portion of the pulse but are in considerable variance on the unloading side. Since the loading calibration was used in reducing entire carbon gage traces and the unloading calibration is not yet available, the laser interferometer traces must be considered more reliable measurements on unloading.

When compared with carbon gage measurements, the interferometer data benefit by three other circumstances that ease interpretation:

(1) The instrumentation plane was negligibly thin (vapor deposited mirror and only one bond), allowing equilibration times to be neglected.

(2) The output signals had better time resolution (displayed over six oscilloscopes).

(3) The onset of signals was unobscured by noise.

The in-material, carbon gage configuration was used in these experiments as backup data. Of necessity, gages were placed behind roughly two-range-thick slabs of PSDB; hence the gage records reflect stress propagation through heated and cold material. From the packaging standpoint, the range-thick PSDB backed with fused quartz is a better configuration for modeling, since the "cold" propagation occurs in a material already well characterized, i.e., fused-quartz buffer.

Thus, considering all the data in these experiments, the quartz-backed interferometer records appear to be the most reliable and the easiest to interpret.

# DISTRIBUTION LIST

DEPARTMENT OF DEFENSE

Director
Defense Advanced Rsch. Proj. Agency
ATTN: Strategic Tech. Office

Defense Communication Engineer Center
ATTN: Code 720, John Worthington

Director
Defense Communications Agency
ATTN: NMCSSC, Code 510

Defense Documentation Center
12 cy ATTN: TC

Director
Defense Intelligence Agency
ATTN: DI-7D
ATTN: DT-1C, Nuc. Eng. Br.
ATTN: DT-2, Wpns. & Sys. Div.

Director
Defense Nuclear Agency
ATTN: STSI, Archives
ATTN: DDST
ATTN: STSP
3 cy ATTN: STTL, Tech. Lib.
3 cy ATTN: SPAS

Dir. of Defense Rsch. & Engineering
ATTN: DD/S&SS
ATTN: AD/OS
ATTN: AD/DS

Commander
Field Command
Defense Nuclear Agency
ATTN: FCTMOF
ATTN: FCPR
ATTN: FCTMD

Director
Joint Strat. Tgt. Planning Staff, JCS
ATTN: JLTW-2
ATTN: JPTM
ATTN: JPTP

Chief
Livermore Division, Fld. Command DNA
Lawrence Livermore Laboratory
ATTN: FCPRL

OJCS/J-5
ATTN: J-5, Plans & Policy, R&D Div.

DEPARTMENT OF THE ARMY

Program Manager
BMD Program Office
ATTN: DACS-BMZ
ATTN: DACS-BMT, John Shea
ATTN: DACS-BMZ-D, Julian Davidson
ATTN: DACS-BMT, Clifford E. McLain

DEPARTMENT OF THE ARMY (Continued)

Commander
BMD System Command
ATTN: BDMSC-TEN, Noah J. Hurst

Dep. Chief of Staff for Rsch., Dev. & Acq.
ATTN: NCB Division

Deputy Chief of Staff for Ops. & Plans
ATTN: Dir. of Chem. & Nuc. Ops.

Commander
Harry Diamond Laboratories
ATTN: DRXDO-RC, Robert B. Oswald, Jr.
ATTN: DRXDO-NP
ATTN: DRXDO-RBH, James H. Gwaltney

Commander
Picatinny Arsenal
ATTN: SMUPA-MD, Henry Opat
ATTN: SARPA-ND-C-T, Donald Miller
ATTN: SARPA-FR-E, Louis Avrami

Commander
TRASANA
ATTN: R. E. DeKinder, Jr.

Director
U.S. Army Ballistic Research Labs.
ATTN: Robert E. Eichelberger
ATTN: DRXBR-TB, J. T. Frasier
ATTN: DRXRD-BVL, William J. Schuman, Jr.

Commander
U.S. Army Mat. & Mechanics Rsch. Ctr.
ATTN: DRXMR-HH, John F. Dignam

Commander
U.S. Army Materiel Dev. & Readiness Cmd.
ATTN: DRCDE-D, Lawrence Flynn

Commander
U.S. Army Missile Command
ATTN: DRSMI-XS, Chief Scientist
ATTN: DRSMI-RRR, Bud Gibson
ATTN: DRS-RKP, W. B. Thomas
ATTN: DRCPM-PE-EA, Wallace O. Wagner

Commander
U.S. Army Nuclear Agency
ATTN: ATCA-NAW

DEPARTMENT OF THE NAVY

Chief of Naval Material
ATTN: MAT 0323, Irving Jaffe

Chief of Naval Operations
ATTN: OP-985D
ATTN: OP-62
ATTN: OP-985

Chief of Naval Research
ATTN: Code 464, Thomas P. Quinn



PRECEDING PAGE BLANK-NOT FILMED

DEPARTMENT OF THE NAVY (Continued)

Director
Naval Research Laboratory
ATTN: Gerald Cooperstein, Code 7770
ATTN: Mario A. Persechino, Code 5180
ATTN: Tech. Lib., Code 2027

Commander
Naval Sea Systems Command
ATTN: 0333A, Marlin A. Kinna

Commander
Naval Surface Weapons Center
ATTN: W. Carson Lyons, Code 323
ATTN: Navy Nuc. Prgms. Off., Code WA-501
ATTN: Leo F. Gowen, Code 2302

Director
Strategic Systems Project Office
ATTN: NSP-272, CDR Leslie Stoessl

DEPARTMENT OF THE AIR FORCE

AF Materials Laboratory, AFSC
ATTN: MAS
ATTN: MBC, Donald L. Schmidt
ATTN: T. Nicholas

AF Rocket Propulsion Laboratory, AFSC
ATTN: RTSN, G. A. Beale

AF Weapons Laboratory, AFSC
ATTN: SUL
ATTN: DYS, Lt E. J. Burns
ATTN: DYV
ATTN: Dr. Minge

Commander
Foreign Technology Division, AFSC
ATTN: TDFBD, J. D. Pumphrey
ATTN: TDPTN

HQ USAF/RD
ATTN: RDPM
ATTN: RDQ
ATTN: RDQSM
ATTN: RD
ATTN: RDQPN

SAMSO/DY
ATTN: DYS

SAMSO/MN
ATTN: MNNR

SAMSO/RS
ATTN: RSSE
ATTN: RSS

Commander in Chief
Strategic Air Command
ATTN: DOXT
ATTN: XPFS

ENERGY RESEARCH & DEVELOPMENT ADMINISTRATION

Division of Military Application
ATTN: Doc. Con. for Res. & Dev. Br.
ATTN: Doc. Con. for CDR Richard E. Peterson
ATTN: Doc. Con. for
Lieutenant Colonel Donald L. McNutt

ENERGY RESEARCH & DEVELOPMENT ADMINISTRATION (Continued)

University of California
Lawrence Livermore Laboratory
ATTN: C. Joseph Taylor, L-92
ATTN: Joseph E. Keller, Jr., L-125
ATTN: G. Staihle, L-24

Los Alamos Scientific Laboratory
ATTN: Doc. Con. for J. W. Taylor
ATTN: Doc. Con. for John McQueen
ATTN: Doc. Con. for R. S. Thurston

Sandia Laboratories
Livermore Laboratory
ATTN: Raymond Ng
ATTN: Doc. Con. for T. Gold
ATTN: Doc. Con. for C. S. Hoyle
ATTN: Doc. Con. for 8131, H. F. Norris, Jr.

Sandia Laboratories
ATTN: Doc. Con. for Albert Chabai
ATTN: Doc. Con. for R. R. Boade
ATTN: Doc. Con. for D. McCloskey

DEPARTMENT OF DEFENSE CONTRACTORS

Aeronautical Rsch. Assoc. of Princeton, Inc.
ATTN: Coleman Donaldson

Aeronutronic Ford Corporation
Aerospace & Communications Ops.
ATTN: P. Spangler

Aerospace Corporation
ATTN: W. Barry
ATTN: R. Allen
ATTN: Richard Crolius, A2, Rm. 1027

Avco Research & Systems Group
ATTN: John Gilmore, E-502
ATTN: John E. Stevens, E-500

Battelle Memorial Institute
ATTN: Merwyn R. Vanderlind
ATTN: W. Pfeifer

The Boeing Company
ATTN: Brian Lempriere

Brown Engineering Company, Inc.
ATTN: Ronald Patrick

Effects Technology, Inc.
ATTN: Robert Wengler

General Electric Company
Space Division
ATTN: G. Harrison
ATTN: Carl Anderson
ATTN: Phillip Cline, Rm. 3700

General Electric Company
TEMPO-Center for Advanced Studies
ATTN: DASIAC

General Research Corporation
ATTN: Robert E. Rosenthal

DEPARTMENT OF DEFENSE CONTRACTORS (Continued)

Institute for Defense Analyses
ATTN: Joel Bengston
ATTN: IDA, Librarian, Ruth S. Smith

Ion Physics Corporation
ATTN: Robert D. Evans

Kaman AviDyne
Division of Kaman Sciences Corp.
ATTN: Norman P. Hobbs

Kaman Sciences Corporation
ATTN: Albert P. Bridges
ATTN: Thomas Meagher
ATTN: Frank H. Shelton
ATTN: Jerry L. Harper
ATTN: John R. Hoffman

Lockheed Missiles & Space Company
ATTN: A. P. Hardt
ATTN: Lloyd F. Chase
ATTN: Raymond R. Capiaux
ATTN: F. G. Borgardt

Martin Marietta Aerospace
Orlando Division
ATTN: Laird Kinnaird

McDonnell Douglas Corporation
ATTN: L. Cohen
ATTN: J. Kirby
ATTN: J. F. Garibotti
ATTN: R. J. Reck

National Academy of Sciences
ATTN: National Materials Advisory Board for
Donald G. Groves

Northrop Corporation
ATTN: Don Hicks

Physics International Company
ATTN: Doc. Con. for James Shea

Prototype Development Associates, Inc.
ATTN: John Slaughter

R & D Associates
ATTN: Albert L. Latter
ATTN: Jerry Carpenter
ATTN: Harold L. Brode
ATTN: F. A. Field

Science Applications, Inc.
ATTN: R. Fisher
ATTN: G. Ray

DEPARTMENT OF DEFENSE CONTRACTORS (Continued)

Science Applications, Inc.
ATTN: J. Courtney

Southern Research Institute
ATTN: C. D. Pear

Stanford Research Institute
ATTN: Donald Curran
ATTN: Herbert E. Lindberg
ATTN: George R. Abrahamson
ATTN: Donald A. Shockey
ATTN: M. J. Ginsberg
ATTN: A. B. Lutze
ATTN: J. P. Wilhelm

Stanford Research Institute
ATTN: Harold Carey

Systems, Science & Software, Inc.
ATTN: G. A. Gurtman
ATTN: Russell E. Duff

Terra Tek, Inc.
ATTN: Sidney Green